The Plant Cell, Vol. 32: 3324–33453345, October 2020, www.plantcell.org © 2020 ASPB.

In Vivo NADH/NAD$^+$ Biosensing Reveals the Dynamics of Cytosolic Redox Metabolism in Plants[OPEN]

Janina Steinbeck,[a] Philippe Fuchs,[a,b] Yuri L. Negroni,[b,c] Marlene Elsässer,[a,b,d] Sophie Lichtenauer,[a] Yvonne Stockdreher,[b] Elias Feitosa-Araujo,[a,e] Johanna B. Kroll,[a] Jan-Ole Niemeier,[a] Christoph Humberg,[a] Edward N. Smith,[f] Marie Mai,[g] Adriano Nunes-Nesi,[e] Andreas J. Meyer,[b] Michela Zottini,[c] Bruce Morgan,[g] Stephan Wagner,[a,b,1] and Markus Schwarzländer[a,2]

[a] Institute of Plant Biology and Biotechnology (IBBP), Westfälische Wilhelms-Universität Münster, D-48143 Münster, Germany
[b] Institute of Crop Science and Resource Conservation (INRES), Rheinische Friedrich-Wilhelms-Universität Bonn, D-53113 Bonn, Germany
[c] Department of Biology, University of Padova, 35131 Padova, Italy
[d] Institute for Cellular and Molecular Botany (IZMB), Rheinische Friedrich-Wilhelms-Universität Bonn, D-53115 Bonn, Germany
[e] Departamento de Biologia Vegetal, Universidade Federal de Viçosa, 36570-900 Viçosa, Minas Gerais, Brazil
[f] Department of Plant Sciences, University of Oxford, Oxford, OX1 3RB, United Kingdom
[g] Institute of Biochemistry, Zentrum für Human- und Molekularbiologie (ZHMB), Saarland University, D-66123 Saarbrücken, Germany

ORCID IDs: 0000-0002-7793-5053 (J.S.); 0000-0001-6379-853X (P.F.); 0000-0002-2163-6687 (Y.L.N.); 0000-0001-8453-1586 (M.E.); 0000-0003-4525-6555 (S.L.); 0000-0003-3556-5936 (Y.S.); 0000-0002-2523-2372 (E.F.-A.); 0000-0003-4652-3598 (J.B.K.); 0000-0002-4081-8101 (J.-O.N.); 0000-0003-3394-9338 (C.H.); 0000-0002-6628-323X (E.N.S.); 0000-0003-1907-7852 (M.M.); 0000-0002-9581-9355 (A.N.-N.); 0000-0001-8144-4364 (A.J.M.); 0000-0001-8930-2969 (M.Z.); 0000-0001-9393-1071 (B.M.); 0000-0001-5369-7911 (S.W.); 0000-0003-0796-8308 (M.S.)

NADH and NAD$^+$ are a ubiquitous cellular redox couple. Although the central role of NAD in plant metabolism and its regulatory role have been investigated extensively at the biochemical level, analyzing the subcellular redox dynamics of NAD in living plant tissues has been challenging. Here, we established live monitoring of NADH/NAD$^+$ in plants using the genetically encoded fluorescent biosensor Peredox-mCherry. We established Peredox-mCherry lines of Arabidopsis (*Arabidopsis thaliana*) and validated the biophysical and biochemical properties of the sensor that are critical for in planta measurements, including specificity, pH stability, and reversibility. We generated an NAD redox atlas of the cytosol of living Arabidopsis seedlings that revealed pronounced differences in NAD redox status between different organs and tissues. Manipulating the metabolic status through dark-to-light transitions, respiratory inhibition, sugar supplementation, and elicitor exposure revealed a remarkable degree of plasticity of the cytosolic NAD redox status and demonstrated metabolic redox coupling between cell compartments in leaves. Finally, we used protein engineering to generate a sensor variant that expands the resolvable NAD redox range. In summary, we established a technique for in planta NAD redox monitoring to deliver important insight into the in vivo dynamics of plant cytosolic redox metabolism.

INTRODUCTION

Nicotinamide adenine dinucleotide (NAD) acts as a central cofactor of redox metabolism across organisms, including plants (Noctor, 2006; Gakière et al., 2018). The oxidized and reduced forms of NAD, NAD$^+$, and NADH, are involved in the electron transfer reactions of a large number of dehydrogenase enzymes, including those of glycolysis, the tricarboxylic acid (TCA) cycle, and the mitochondrial electron transport chain (mETC; Fernie et al., 2004). NAD also regulates enzyme activity, and NAD$^+$ is required for the de-acetylation of histones and metabolic proteins (Møller et al., 2020). Modification of cellular NAD homeostasis can have pronounced, but remarkably specific, effects on plant hormone regulation, reproductive efficiency, and guard cell density, providing a link between redox metabolism and plant developmental programs (Hashida et al., 2007, 2010; de Souza Chaves et al., 2019; Feitosa-Araujo et al., 2020; Wei et al., 2020). Phosphorylation of NAD$^+$ by NAD$^+$ kinase produces NADP$^+$ and in analogy, phosphorylation of NADH by NADH kinase produces NADPH (Li et al., 2018). NADP has vital roles in anabolic metabolism, such as photosynthetic carbon fixation, and it is an important electron donor for thiol-based redox regulation and antioxidant defense (Møller et al., 2020). Consequently, NAD constitutes a backbone of cellular redox metabolism.

Since the NAD redox state is directly coupled to the flux through many metabolic reactions and has fundamental impacts on fluxes throughout the entire plant metabolic network, extremes of NAD oxidation and reduction can disrupt metabolism. When oxidative phosphorylation capacity is limited, for example, under hypoxia,

[1] Current address: Max-Planck-Institute for Plant Breeding Research, D-50829 Cologne, Germany.
[2] Address correspondence to markus.schwarzlander@uni-muenster.de. The author responsible for distribution of materials integral to the findings presented in this article in accordance with the policy described in the Instructions for Authors (www.plantcell.org) is: Markus Schwarzländer (markus.schwarzlander@uni-muenster.de).
[OPEN]Articles can be viewed without a subscription.
www.plantcell.org/cgi/doi/10.1105/tpc.20.00241

IN A NUTSHELL

Background: All organisms rely on their cellular metabolism to live, develop, grow, and procreate. Metabolism provides the energy, building blocks, and reductant (i.e., electrons) needed for these activities. A major proportion of the total electron flux of most cells runs through the nicotinamide adenine dinucleotide (NAD) redox system. NAD acts as a co-factor in central metabolism, shuttling electrons from and to pathways as central as respiration and glycolysis. In addition, NAD plays important roles in regulation through posttranslational protein modification and signaling crosstalk with hormonal pathways.

Question: Despite our exquisite mechanistic understanding of NAD biochemistry, its redox dynamics in living plants has been hard to assess directly. Yet, resolving the defining differences between tissues, cells, and cell compartments is critical if we are to integrate our biochemical understanding into a meaningful physiological framework. This is particularly limiting in green plant cells where two major bioenergetic redox machineries operate.

Findings: We explored the in vivo NAD redox dynamics in the model plant *Arabidopsis thaliana* using a fluorescent protein sensor called Peredox-mCherry. Focusing on the cytosol, the central compartment in which redox metabolism from the different cell organelles is integrated, we observed that NAD redox status is remarkably flexible in living plants, despite being a central hub in the metabolic network. We mapped the cytosolic NAD redox landscape in different cell and tissue types and monitored tissue responses to environmental cues such as light, external sugar supply, respiratory dysfunction, hypoxia, and elicitor exposure. We also engineered a new sensor variant that expands the range in which NAD redox measurements can be performed.

Next steps: In vivo monitoring of NAD redox dynamics opens the door to answering several long-standing questions, such as the relationship between cellular redox metabolism and developmental programs and the spatiotemporal signatures of NAD under stress conditions or during immune responses.

the resulting Pasteur effect includes a boost in glycolytic flux to maintain ATP production. However, this leads to a high rate of NAD^+ reduction and requires the activation of fermentation of pyruvate to ethanol or lactate (Tadege et al., 1999; António et al., 2016). Fermentation allows NADH to be re-oxidized to avoid large-scale disruption of metabolic function, albeit at the major cost of inefficient carbon and energy use, highlighting the vital significance of NAD redox maintenance. A similar function is fulfilled by the alternative respiratory pathways in plant mitochondria, including the alternative NADH dehydrogenases and alternative oxidase (van Dongen et al., 2011). Although oxidation of NADH via the alternative respiratory pathway still requires oxygen as a terminal electron acceptor, it provides a mechanism for maintaining NAD redox balance independent of the capacity of the classical respiratory pathway, ATP-synthase activity, and adenylate charge (Wagner et al., 2018).

The redox state of the cellular NAD pools can fluctuate; such changes have been associated with a variety of physiological conditions and stress situations (Hashida et al., 2007; Hunt et al., 2007; Schippers et al., 2008; Pétriacq et al., 2016). NAD redox management by the plant cell is likely to include moving major quantities of reducing equivalents between different cell compartments. While NAD^+ can be transported across the membranes of different cellular organelles, including those of the chloroplast, mitochondrion, and peroxisome (Palmieri et al., 2009; Bernhardt et al., 2012; de Souza Chaves et al., 2019; Luo et al., 2019; Feitosa-Araujo et al., 2020), there is no evidence for any efficient direct intracellular transmembrane transport of NADH. This highlights the need for metabolite shuttles to move redox equivalents between intracellular compartments. Among different mechanisms, the malate valves that operate between the cytosol and the plastid stroma, mitochondrial matrix, and peroxisomal lumen have attracted major attention due to their potential to reach major flux rates in plant cells (Selinski and Scheibe, 2019). The enzymes involved and their regulation have been studied intensely, and a set of dicarboxylate carriers present in the inner mitochondrial membrane, the inner plastid envelope, and the peroxisome membrane have been implicated in the required transmembrane transport (Weber and Flügge, 2002; Renné et al., 2003; Lee and Millar, 2016). The directionality of shuttling and the flux rates involved in vivo have remained less clear, however. Both parameters strongly depend on the exact metabolic situation, making it likely that they are highly variable depending on developmental and environmental conditions. Even assuming a metabolic steady state, any reliable estimation of flux rates through the redox shuttle systems in the living cell remains extremely difficult, even at a qualitative level. Major advances have recently been made by metabolic modeling (Shameer et al., 2019), while a reliable means for direct experimental assessment remains to be established.

Despite the central role of plant NAD in metabolism and its emerging roles in regulation and signaling, the current understanding of NAD redox dynamics in vivo, NAD compartmentation, and redox exchange between the cellular compartments remains surprisingly sketchy. It has been technically challenging to monitor NAD redox dynamics in vivo. Typically, $NADH/NAD^+$ ratios are determined by biochemical analyses of whole-cell extracts, in which metabolite pools from different cell compartments have been mixed. Such analyses therefore offer little insight into subcellular compartment–specific $NADH/NAD^+$ dynamics inside living cells. Hans Krebs established a method for indirectly deducing cytosolic free $NADH/NAD^+$ ratios from metabolite ratios more than 50 years ago. Such analysis is typically based on measuring pyruvate and lactate concentrations and the assumption of their equilibrium in situ (Williamson et al., 1967; Sun et al., 2012). This method has been widely exploited, but dynamic in vivo measurements have remained nonaccessible for many systems since they are technically highly demanding (Christensen et al., 2014). Although dynamic in vivo measurements of NAD(P)H

concentrations are possible based on the autofluorescence of the reduced species, as proposed nearly 60 years ago (Chance et al., 1962), for plants, this remains limited to isolated organelles due to interfering autofluorescence from other cellular components and the high intensity of UV illumination required (Kasimova et al., 2006). Even in systems that allow measurement of NAD(P)H autofluorescence, NAD(P)H in the mitochondrial matrix dominates the cellular signals, thereby impeding attempts to assess NAD(P)H dynamics in other cell compartments. Furthermore, NADH shows the same spectral properties as NADPH, resulting in a mixed readout of both independent pools. An elegant approach that was developed to separate both species using their different fluorescence lifetimes (Blacker et al., 2014) offers several advantages, but it does not overcome the hurdle of distinguishing NAD redox status between cell compartments and has not been optimized for plants.

Several fluorescent protein–based NAD biosensors were recently developed, providing novel insight into NAD dynamics in mammalian, fungal, and bacterial systems (Hung et al., 2011; Zhao et al., 2011, 2015; Bhat et al., 2016; Cambronne et al., 2016; Ishikawa et al., 2017; Tejwani et al., 2017; Hartmann et al., 2018). One of these sensors, Peredox-mCherry, was designed using a T-Rex NAD^+- and NADH binding protein linked to the blue-green fluorescent protein tSapphire (tS; Hung et al., 2011). The binding of NADH to this sensor causes a steric rearrangement that leads to an increase in fluorescence intensity. NAD^+ competes for the binding site, but its binding has a neutral impact on the fluorescence emission intensity. As a result, tS fluorescence intensity depends on the ambient NADH/NAD^+ ratio. For internal normalization C-terminal fusion with mCherry (mC), which is inert to the NADH/NAD^+ ratio, has been used to generate a ratiometric sensor construct. The pH sensitivity of the sensor was minimized by targeted mutagenesis (Hung et al., 2011).

Alternative NAD sensors include Frex, FrexH, RexYFP, and SoNar (Zhao et al., 2011, 2015; Bilan et al., 2014; for a review, see Bilan and Belousov, 2017). Frex and FrexH provide a readout for absolute NADH levels but show pronounced pH sensitivity; SoNar allows NADH/NAD^+ measurements with a strongly increased spectroscopic response range but is also highly pH sensitive. A sensor for NAD^+ concentrations based on cpVenus fused with a bipartite NAD^+ binding site of a bacterial DNA ligase was recently developed and used in the mitochondrial matrix (Cambronne et al., 2016), and a semisynthetic fluorescent NAD^+ biosensor, NAD-Snifit, was subsequently introduced (Sallin et al., 2018). Very recently, a sensor named FiNAD was developed that responds to NAD^+/AXP ratios, where AXP is the pool of ATP and ADP (Zou et al., 2020). Despite the important advances that NAD biosensing has delivered in mammalian and fungal systems, and the potential to gain insight into the flexibility of subcellular plant metabolism, these NAD biosensors have not been established in plants. One recent study made use of NAD sensing as part of a multiparameter approach for analyzing hypoxia physiology, but without specific development of the methodology (Wagner et al., 2019). During the revision of this work, a study was published exploiting SoNar in combination with a pH correction regime for NAD redox monitoring in the cytosol and the chloroplast stroma of Arabidopsis (*Arabidopsis thaliana*; Lim et al., 2020).

Here, based on the properties of the currently available biosensors, we focused on Peredox-mCherry to establish a method for sensing the NAD redox status in living plants. Peredox-mCherry was the only sensor that (1) provides an integrated measurement of NAD redox status, as opposed to NAD^+ or NADH concentration; (2) can be measured in a self-normalizing ratiometric manner; and (3) was reported to be largely pH inert. First, we expressed Peredox-mCherry in the cytosol to generate stable Arabidopsis biosensor lines. Second, we validated the biophysical and biochemical characteristics of Peredox-mCherry in vitro under conditions that are expected to be relevant in planta. Third, we imaged the NAD redox landscape in living Arabidopsis seedlings to reveal tissue-specific differences and gradients in cytosolic NAD redox status. Analysis of etiolated seedlings demonstrated that the establishment of these gradients is flexibly modified depending on developmental status and the environment. Fourth, we investigated the impact of short-term transitions in photosynthetic and respiratory activity, as well as external carbon availability and elicitor exposure, on cytosolic NAD redox status and resolved the kinetic responses of NAD redox metabolism. Finally, we engineered a sensor variant for use in more reducing NAD redox environments to provide a usable toolkit for NAD redox monitoring in plants.

RESULTS

Arabidopsis Lines Expressing an NAD Redox Sensor in the Cytosol

To perform NAD redox measurements in living plants, we generated Arabidopsis lines that expressed Peredox-mCherry constitutively under the control of the *UBIQUITIN10* promoter in the cytosol. We selected three independent lines that showed intense fluorescence signal, which localized to the peripheral cytosol, trans-vacuolar strands, and nucleoplasm (Figures 1A to 1E; Supplemental Figures 1A and 1B). When we attempted to generate analogous sensor lines for the mitochondrial matrix, selection for transformed individuals yielded no results. This is in line with the previous observation that the import of large biosensor constructs into mitochondria compromises plant development (De Col et al., 2017). Even though severe growth phenotypes can also occur for specific biosensors expressed in the cytosol, we observed no phenotypic differences at the whole-plant level between the homozygous Peredox-mCherry lines and the wild type without sensor expression. Quantitative phenotyping of rosette size, inflorescence height, and root length (Figures 1F to 1I; Supplemental Figures 1C and 1D) confirmed that sensor expression did not induce apparent phenotypes. Homozygous line #1 was an exception, as it displayed slightly increased inflorescence height and root growth compared to the wild-type control, perhaps due to the specific location of the T-DNA insertion rather than sensor expression. We did not observe any obvious reproductive phenotypes, but the potential impact on a specific parameter of interest should be assessed when the lines are used in future studies.

pH Stability and Specificity for NAD Make Peredox-mCherry Useful for in Planta Measurements

To allow for reliable interpretation of in planta sensor measurements, we sought to obtain additional insight into the specificity of

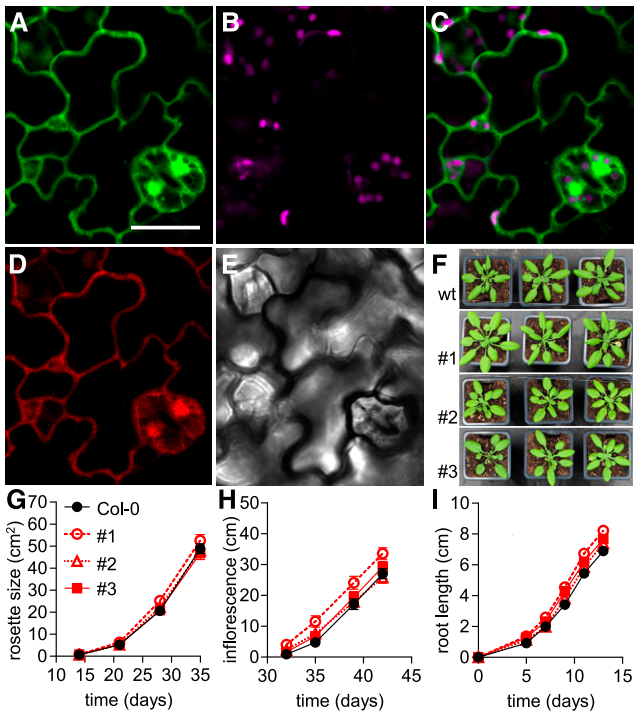

Figure 1. Peredox-mCherry Expression in Arabidopsis.

(A) to **(F)** Subcellular localization of Peredox-mCherry in abaxial epidermal cells of cotyledons of 5-d-old Arabidopsis seedlings. **(A)** tS fluorescence (green): excitation, 405 nm; emission, 517.5 ± 7.5 nm. Bar = 20 μm. **(B)** Chlorophyll fluorescence (magenta): excitation, 575 nm; emission, 675 ± 25 nm. **(C)** Overlay of tS and chlorophyll fluorescence. **(D)** mC fluorescence (red): excitation, 575 nm; emission, 612.5 ± 7.5 nm. **(E)** Transmission of the tS channel. Six analogous cotyledon epidermal areas were assessed in each of four seedlings. Consistent localization was observed in all three Peredox-mCherry lines. **(F)** Representative phenotypes of 28-d-old Arabidopsis plants of three independent homozygous biosensor lines (#1, #2, and #3) grown side by side with wild-type (wt) control (Col-0) plants in soil under long-day conditions.

(G) Rosette leaf area of the three sensor lines compared to Col-0 quantified across the plant growth period in soil (n = 19 to 20, means ± SE).

(H) Inflorescence height of the plants (n = 19 to 20, means ± SE).

(I) Vertical primary root length on half-strength MS medium supplemented with 1% (w/v) Suc and 1% (w/v) agar (n = 25, means ± SE). Two-way ANOVA followed by Dunnett's multiple comparisons test for data in **(G)** to **(I)**. Note that line #1 showed significantly increased inflorescence height and root length ($P < 0.001$) compared to Col-0; rosette size of line #1 and all comparisons of lines #2 and #3 were not significantly different from the Col-0 control ($P > 0.05$; Supplemental Data Sets 1A to 1C).

the sensor response, complementing previous in vitro analyses of the Peredox-mCherry protein (Hung et al., 2011; Tejwani et al., 2017; Hartmann et al., 2018). In particular, we were interested in sensor specificity to NAD versus NADP, as well as changes in ambient pH and sensor response kinetics, to appropriately consider their influence on in planta measurements. The model of Peredox-mCherry function suggests that the homodimeric Rex domain undergoes a conformational change in response to NADH binding, thereby increasing the fluorescence intensity of the circularly permuted GFP-derived protein tS, which is integrated between the two Rex monomers (Figure 2A; Hung et al., 2011). The fluorescence spectra of the C-terminal mC remain unaffected, allowing the tS signal to be internally normalized. Since NAD^+ binds to the sensor, but does not affect its fluorescence, the tS/mC fluorescence ratio reports on the NADH/NAD^+ ratio rather than NADH concentration (Hung et al., 2011).

To obtain purified recombinant Peredox-mCherry sensor protein, we optimized the expression conditions, *Escherichia coli* strain, and protein storage conditions (Supplemental Figure 2). Measuring the emission spectrum of the purified sensor protein confirmed a ratiometric shift in response to NADH, with a dynamic range (δ) of 2.2 (Figure 2B; Supplemental Figure 3). tS fluorescence increased in response to NADH, but not to NAD^+ (excitation at 400 nm, emission peak at 513 nm), while mC fluorescence remained unchanged (excitation at 580 nm, emission peak at 605 nm). Medium NAD^+ concentrations of 500 μM were chosen to approximate the lower end of the range of cytosolic NAD^+ concentrations previously measured from extracts of mesophyll protoplasts (Igamberdiev and Gardeström, 2003; Gakière et al., 2018). Adjusting NADH concentrations from 0 to 100 μM in the presence of 500 μM NAD^+ led to a sigmoidal increase in the tS/mC fluorescence ratio, with a K_d-value for NADH of 1.2 ± 0.15 μM (Figure 2C; Supplemental Figures 3A and 3B). Cytosolic NADH concentrations of pea (*Pisum sativum*) leaf protoplasts in the dark were previously measured at 18 ± 14 μM NADH (Igamberdiev and Gardeström, 2003). A response to NADPH in the presence of 150 μM $NADP^+$ (previously estimated as the concentration of the cytosolic $NADP^+$ pool; Igamberdiev and Gardeström, 2003) was only observable at concentrations two orders of magnitude higher (K_d for NADPH, 531 ± 12 μM; Figure 2C; Supplemental Figures 3C and 3D). As a result, the in planta response of Peredox-mCherry is likely to be specific to NAD redox status and will most likely not be affected by the NADP pool under physiological conditions. tS/mC was largely stable within the physiologically relevant pH range from 6 to 9 (Figure 2D), as assessed for three different conditions of NAD^+ and NADH binding (Figure 2C): occupied by NAD^+ (0.1 μM NADH, 500 μM NAD^+), occupied by NADH (5 μM NADH, 500 μM NAD^+), and at similar occupancy by NAD^+ and NADH (1.2 μM NADH, 500 μM NAD^+; Figure 2D). The residual pH dependency observed was minor compared to the NAD redox response. The absence of direct effects of pH on the fluorophores is particularly important, since pH can fluctuate substantially in the plant cytosol (e.g., Felle, 2001; Behera et al., 2018), and pH stability represents a decisive advantage over several other NAD sensors (Zhao et al., 2011, 2015).

Finally, we investigated the binding and dissociation kinetics of NADH to and from the sensor protein in the presence of NAD^+ as a competitor for binding (Figure 2E). The tS/mC ratio values were also $\log_{10}$ transformed, allowing us to accurately represent the ratio variance and to restore symmetry of the ratio data; all subsequent data are presented in this manner. Equilibration of the sensor protein with NAD^+ prior to NADH addition ensured that no NADH was bound when the assay was started. At NADH addition (1 μM), tS/mC increased to half of the full response amplitude in 73 ± 1 s, whereas the dissociation of NADH, as triggered by the addition of NAD^+ (500 μM), was slower and required 211 ± 7 s to reach half of the response amplitude (a more detailed analysis of the binding and dissociation kinetics for different NADH concentrations is

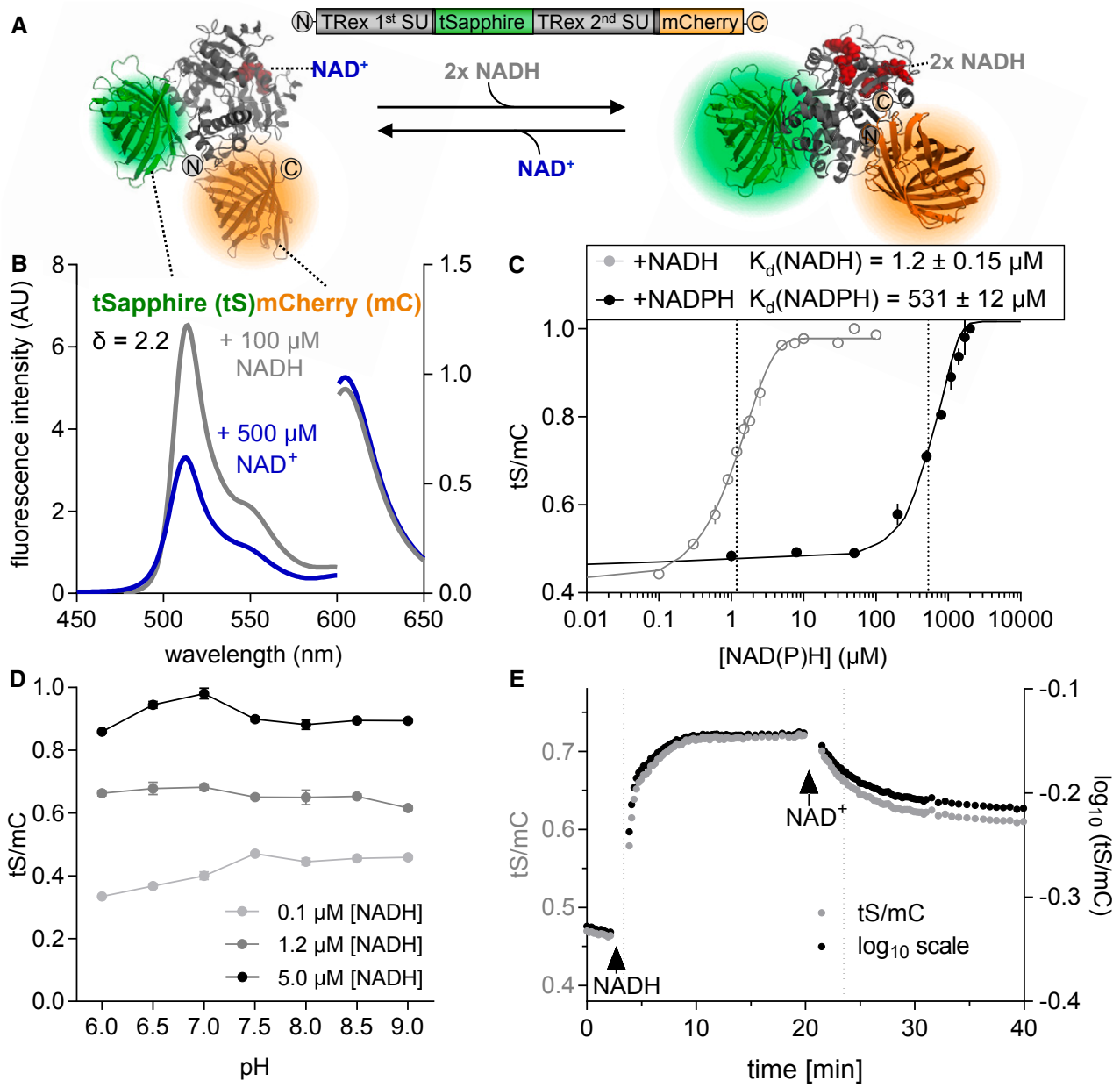

Figure 2. Characteristics of Purified Recombinant Peredox-mCherry Protein.

(A) Hypothetical structural model of Peredox-mCherry. tS (Protein Data Bank [PDB]: 3evp, green) is interposed between two Rex subunits (SU; PDB: 2vt2 and 1xcb, gray). The binding of NADH (red, right) increases tS fluorescence, while NAD^+ binding does not (red, left). tS signal is normalized by the mC (PDB: 2 h5q, orange) signal, which is unresponsive to NAD status. mC is fused to the C terminus of the second Rex domain.

(B) Emission spectra of tS (excitation at 400 ± 5 nm, left *y* axis) and mC (excitation at 580 ± 5 nm, right *y* axis) in arbitrary units (AU) × 10^3 after the addition of 500 µM NAD^+ (blue) or 500 µM NAD^+ plus 100 µM NADH (gray). The spectroscopic dynamic range (δ) was calculated from the tS/mC ratios at the respective emission maxima of the two fluorophores (tS, 513 ± 5 nm; mC, 610 ± 5 nm) for the NAD^+-bound and NADH-bound sensor. Sensor protein concentration: 0.025 µg/µL in Tris-HCl, pH 7.5 (also for subsequent measurements unless otherwise stated).

(C) Ratiometric response of Peredox-mCherry to different NADH and NADPH concentrations in the presence of 500 µM NAD^+ and 150 µM $NADP^+$, respectively ($n = 3$, mean ± SD), pH 7.5. The ratio values were normalized to the highest ratio (set to 1) to allow comparison of NADH and NADPH binding (corresponding tS and mC spectra are presented in Supplemental Figures 3A to 3D). Data were fitted to a sigmoidal interpolation (Supplemental Data Set 1D). Dotted lines indicate K_d-values for NAD(P)H.

(D) Response of Peredox-mCherry to different pH values. Sensor protein was equilibrated with three different NADH concentrations (0.1, 1.2, and 5 µM) in the presence of 500 µM NAD^+ to achieve low, mean, and high NADH/NAD^+ binding at different pH values (6.0 to 9.0, $n = 3$, mean ± SD). The tS/mC fluorescence ratios were determined as in **(C)** at the indicated pH of the buffer (Bis-Tris for pH 6.0 to 7.0 and Tris-HCl for pH 7.5 to 9.0).

presented in Supplemental Figures 3E and 3F). Consequently, the binding and dissociation kinetics may limit the ability of the sensor to monitor very rapid NAD redox dynamics. While the delayed sensor response represents a disadvantage that needs to be considered when interpreting the temporal responses of in vivo experiments, this behavior will also extend the time window in which very rapid metabolic transitions between a more oxidized and a more reduced NAD pool (and vice versa) can be resolved. Endogenous proteins can also show low rates in NAD binding and NAD dissociation, which has given rise to the concept of bound and free NAD pools. Here, Peredox-mCherry makes no exception and provides insight into NAD redox dynamics, as occurs for endogenous proteins with similar binding and dissociation rates.

Peredox-mCherry Reports on Changes in Net NAD Reduction and Oxidation by Mitochondrial Malate Metabolism ex Situ

Since NADH and NAD^+ represent a central redox couple of respiratory metabolism, we aimed to explore how mitochondrial metabolic activities can affect NAD redox status depending on substrate availability. We recently established an ex situ strategy to assess mitochondria-mediated changes in ATP (De Col et al., 2017), and we have adapted that strategy here to monitor NAD redox dynamics as mediated by malate metabolism. We supplemented suspensions of Arabidopsis seedling mitochondria, purified Peredox-mCherry protein, and NAD^+ (500 μM) with different concentrations of malate (Figure 3A) to test the ability of the NAD redox sensor to report NAD redox changes from a complex organelle system. Malate is readily imported into the matrix of plant mitochondria, where it is metabolized by malate dehydrogenase (MDH) and malic enzyme at high capacity coupled to the reduction of NAD^+ (Zoglowek et al., 1988; Fuchs et al., 2020). Any efficient direct export of NADH from intact mitochondria into the medium is unlikely (Douce et al., 1973; Palmieri et al., 2009). We reasoned that the rupture of a fraction of the mitochondria would bring matrix enzymes in direct contact with NAD^+ and the sensor in the medium; alternatively, MDH activity is typically also present at the outer mitochondrial membrane of isolated mitochondria. Once generated, NADH can be re-oxidized by the NADH dehydrogenases of the mETC (Rasmusson et al., 2004).

The addition of malate at 0.5, 1.5, and 10 mM indeed resulted in a dose-dependent reduction of the NAD pool, as indicated by the increase in the $\log_{10}$(tS/mC) signal ratio by 0.10, 0.26, and 0.31, respectively (Figure 3B), with a corresponding spectroscopic dynamic range of 2.04, that is, similar to the dynamic range determined by the external addition of NADH (Figure 2C). MDH activity likely accounted for most of the reduction of NAD^+ to

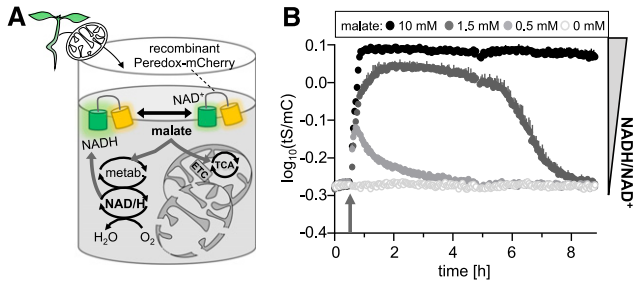

Figure 3. Peredox-mCherry–Based ex Situ Monitoring of NAD Redox Changes Driven by Mitochondrial Malate Metabolism.

(A) Mitochondria isolated from the 16-d-old Arabidopsis wild-type seedlings were mixed with purified recombinant Peredox-mCherry protein (0.5 μM) and NAD^+ (500 μM) in basic incubation medium, pH 7.5, and supplemented with malate. The sensor protein provides a readout for redox changes in the NAD pool in the medium. ETC, electron transport chain; metab., metabolism.

(B) NAD redox dynamics in response to the addition of malate at three different concentrations compared to the control (arrow). tS/mC ratio indicates redox changes in the NAD pool in the medium. Fluorescence emission was measured in each well of a multiwell plate every 149 s and $\log_{10}$ transformed. Averaged sensor ratios are plotted after correction of background signal. Excitation, 400 ± 10 nm (tS) and 570 ± 10 nm (mC); emission, 515 ± 7.5 nm (tS) and 610 ± 5 nm (mC). $n = 4$, mean + SD.

NADH, linked to malate oxidation, since the assay pH is far above the pH optimum of malic enzyme. The re-oxidation of the NAD pool, as indicated by a decreasing tS/mC, can be explained by the notion that the reaction catalyzed by MDH reached equilibrium (note that the reaction has a very low equilibrium constant favoring malate and NAD^+ over oxaloacetate and NADH; Coleman and Palmer 1972). Since further malate oxidation and NAD^+ reduction are readily inhibited through the accumulation of oxaloacetate and NADH, net oxidation of NADH can occur via a reaction mediated by the activity of mETC NADH-dehydrogenases, including complex I and the alternative NADH dehydrogenases (Rasmusson et al., 2004). Even though malate will not be fully depleted, the added malate concentration determines how long it will take until equilibrium will be reached and net NADH oxidation can commence. The NAD redox status is therefore set by the rates of NAD^+ reduction and NADH oxidation in the ex situ model system. Since net reduction and net oxidation dominate at different time windows of the assay, which can be modified by changing the amount of added substrate, the dose-dependent dynamics verify the ability of Peredox-mCherry to report NAD redox dynamics, like those that can be induced by changes in the fluxes through respiratory carbon metabolism.

Figure 2. (continued).

(E) NADH binding to and dissociation from Peredox-mCherry in vitro. Time resolved tS/mC (gray, left *y* axis) and corresponding $\log_{10}$-transformed ratio changes (black, right *y* axis) in response to NADH (1.2 μM, first arrow) in the presence of 500 μM NAD^+ and to further NAD^+ addition (500 μM, second arrow). Dotted lines indicate time to reach half of the response amplitude at NADH or NAD^+ addition (linear regression analysis of $\log_{10}$-transformed ratios (one-phase decay fit; Supplemental Data Set 1E). Fluorescence emission was measured by multiwell plate reader–based fluorimetry in each well every 13 s. Excitation, 400 ± 10 nm (tS) and 570 ± 10 nm (mC); emission, 520 ± 5 nm (tS) and 610 ± 5 nm (mC). The assay was independently repeated three times with consistent results.

A Seedling-Scale Atlas of the Cytosolic NAD Redox Landscape

We next sought to explore how heterogeneous the cytosolic NAD redox status is across tissues. This issue has been unclear because NAD measurements in tissue extracts can only provide an average value across cell compartments, cell types, and tissues, resulting in the loss of information about specific tissues and cell types. To address this issue, we performed confocal laser scanning microscopy analysis of cytosolic NAD redox state across entire 5-d-old Arabidopsis seedlings (Figure 4A). The $\log_{10}$(tS/mC) ratios ranged from 0.38 ± 0.06 (indicative of a highly reduced NAD state) in the root epidermis down to 0.005 ± 0.049 (indicative of a highly oxidized NAD state) in the area of the leaf primordia in the vicinity of the shoot apical meristem (SAM) region (Figures 4A and 4B). The resulting $\log_{10}$-response range of 0.37 (δ = 2.35) equals the theoretical range of the sensor determined in vitro (Figure 2C), suggesting that the sensor affinities for NADH and NAD^+ are well matched with the cytosolic NAD redox environment in planta, but also that the NAD pool in the tissues with the lowest and highest values may adopt redox states beyond the sensitivity range of the sensor. To control for potential artifacts of steady state measurements through the contributions of tissue autofluorescence, we also imaged wild-type seedlings without sensor as a control (Supplemental Figure 4A). The average contribution was minor, suggesting that meaningful measurements can be obtained without further correction (autofluorescence contributions empirically determined for representative seedlings of line #3 were 2.9% for tS and 0.4% for mC signal; Supplemental Figure 4A). We then explored potential differences in sensor status between the cytosol and the nucleoplasm. The assessment of guard cells, pavement cells, and hypocotyl epidermal cells did not reveal any difference, which is in line with the finding that the sensor protein showed efficient diffusion across the nuclear pores (Supplemental Figure 4B).

The tS/mC ratios of cotyledons and hypocotyl were low (more oxidized NAD pool) relative to the higher tS/mC ratios in the root (more reduced NAD pool; Figures 4A and 4B). The observed gradient of increasing NAD reduction from shoot to root negatively correlates with the gradient in the concentrations of cytosolic $MgATP^{2-}$, which are high in shoots and lower in roots, as detected with the biosensor ATeam 1.03 nD/nA (De Col et al. 2017). The epidermis displayed a more reduced NAD pool compared to the vasculature in both cotyledons (epidermis, 0.13 ± 0.03; vasculature, 0.06 ± 0.03) and roots (epidermis, 0.21 ± 0.09; vasculature, 0.17 ± 0.08). No such differences were detected in the hypocotyl (epidermis, 0.14 ± 0.05; vasculature, 0.10 ± 0.07; Figures 4A and 4B).

By contrast, the NAD pools in 5-d-old etiolated seedlings grown in the dark under otherwise identical conditions showed a general shift toward oxidation. This shift was most pronounced in root tissues, which markedly decreased the gradient in the whole plant from shoot and root (Figures 4B and 4C). This reveals that even during early seedling establishment, when the photoautotrophic lifestyle is not yet fully functional, the status of photomorphogenesis and/or establishment of the photosynthetic machinery of the aerial organs has a strong impact on the metabolism of the heterotrophic root tissues.

Establishment of Parallelized Fluorimetry to Monitor Cytosolic NAD Redox Dynamics

The tissue-specific differences in NADH/NAD^+ ratios suggest that different ratios can be adopted by cells without crossing the limits of normal NAD redox physiology. To explore how volatile cytosolic NAD redox status really is, we aimed to study responses to external changes in a dynamic fashion using leaf tissue as a model. Plate reader–based multiwell fluorimetry allows reversible biosensor responses to be recorded over time, with parallelized controls and replicates, and is particularly well suited for monitoring the impact of external treatments at the tissue and organ level (De Col et al., 2017; Nietzel et al., 2019; Wagner et al., 2019). The ratiometric nature of the sensor is critical, since it provides internal normalization for variability in sensor expression levels as well as tissue amounts and positioning, but it requires the sensor signal to be sufficiently high in order to be reliably discriminated from the background. To test whether the Peredox-mCherry sensor lines pass this criterion, we assessed the degree of interference from endogenous fluorescence with the sensor signals in situ in leaf discs of 5-week-old Arabidopsis plants. Two-dimensional spectra of excitation and emission from the three independent Peredox-mCherry lines compared to the wild type revealed the characteristic spectra of tS and mC (Supplemental Figure 5), which clearly resembled the in vitro spectra of the sensor (Figure 2B). The sensor maxima were absent in the wild-type control, further indicating that autofluorescence was low in the relevant spectral regions. Importantly, chlorophyll fluorescence was spectrally well separated, and the emission peaks of tS and mC generally showed a favorable signal-to-noise ratio (e.g., 7.5:1 at 514 nm [tS] and 28:1 at 605 nm [mC] emission of line #3 compared to non-transformed wild type Columbia-0 [Col-0]; Supplemental Figures 5A and 5B).

In Vivo Monitoring of NAD Redox Dynamics in Response to Changes in Illumination, Respiration, and Carbon Supply

We next aimed to explore the responses of cytosolic NAD redox status to external transitions with known effects on intracellular energy and redox physiology. To obtain insight into inter-compartment redox exchange, we made use of the exclusive cytonuclear sensor localization and applied stimuli with primary effects on the chloroplasts and mitochondria, respectively (Figure 5A). We first used illumination as a stimulus and performed dark–light transition experiments to trigger photosynthesis (Figure 5B). Since fluorescence readings are not possible during illumination, we recorded tS/mC in the periods before and after light exposure. Interestingly, illumination led to a pronounced reduction of the cytosolic NAD pool, as indicated by the recovery of tS/mC (re-oxidation of the NAD pool) directly after the light treatment. The relatively slow dissociation kinetics of NADH from the Peredox-mCherry protein (Figure 2E) likely underestimate the speed of the redox changes but is helpful for monitoring the transitions, where the true starting values in the light are not accessible. The presence of the photosystem II inhibitor 3-(3,4-dichlorophenyl)-1,1-dimethylurea (DCMU; Wilcox and Moreland, 1969) abolished the reduction of the cytosolic NAD pool by light, indicating that active photosynthetic electron transport in the

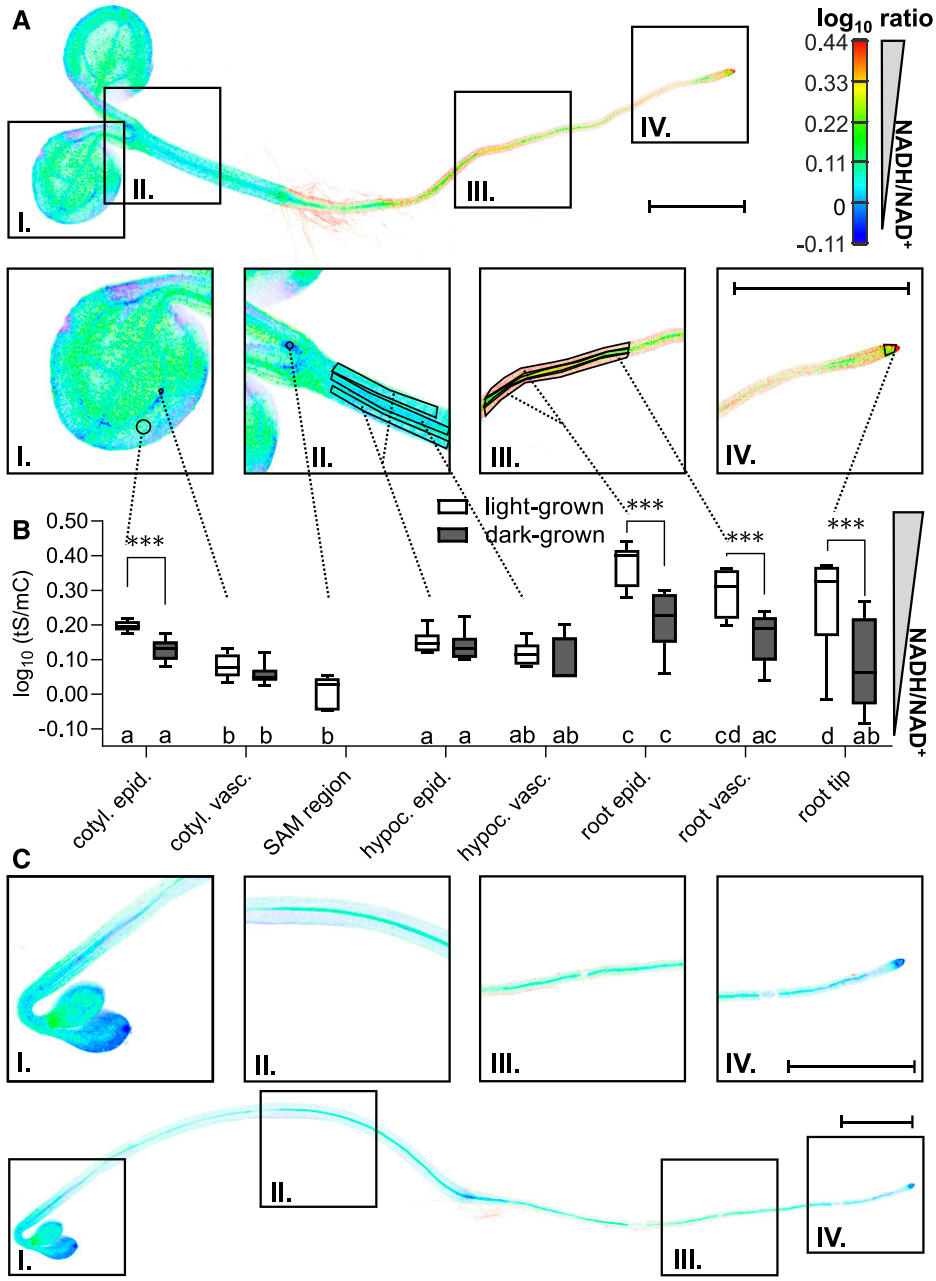

Figure 4. Peredox-mCherry Status in Different Tissues of an Arabidopsis Seedling.

(A) tS and mC fluorescence of 5-d-old seedlings was recorded by confocal laser scanning microscopy, and the ratio is plotted in false colors (sequential excitation, 405 and 570 nm; emission recorded at 517.5 ± 7.5 and 612.5 ± 7.5 nm, respectively), where high tS/mC (red) corresponds to reduced NADH/NAD^+ steady state levels. The seedlings were kept in the dark for 120 min before image acquisition to avoid potential effects of active photosynthesis. A representative seedling of line #3 is shown. In the close-ups, tS/mC ratios were analyzed in the indicated ROIs, with 1 out of 10 randomly distributed circular ROIs across a cotyledon shown to facilitate visibility of the actual differences. Enlarged are I, cotyledon; II, hypocotyl and shoot apical meristem (SAM) region; III, root; and IV, root tip. Note that the SAM region was not exposed in the etiolated seedlings and was hence not analyzed to avoid mechanically invasive sample preparation. Bars = 1 mm. cotyl., cotyledon; epid., epidermis; hypoc., hypocotyl; vasc., vasculature.

(B) Comparison of the tS/mC ratios of light-grown **(A)** versus etiolated seedlings in the dark **(C)**, and comparison of tissue-specific differences in the seedlings under each condition. Seedlings of line #3 were used for the analysis; $n = 6$, whiskers represent minimum and maximum values. Statistical analysis with a two-way ANOVA followed by the Tukey test; different letters indicate significant differences between ROIs of seedlings under the indicated growth condition ($P \leq 0.05$), asterisks indicate significant differences between light-grown versus etiolated seedlings for the indicated ROI (***$P \leq 0.001$; Supplemental Data Set 1F).

(C) Confocal microscopy analysis of a representative 5-d-old seedling etiolated in the dark. For statistical comparison of the NAD redox state to light-grown seedlings **(B)**, ROIs were selected analogously to **(A)**. Bars = 1 mm.

thylakoids is causative for NAD reduction in the cytosol and implying that reducing equivalents are exported from the chloroplast to the cytosol.

We then investigated the effect of carbon status (in the form of free Suc) on cytosolic NAD redox status, as we hypothesized that the tissue-specific differences in the cytosolic NAD redox state (Figure 4) between the vasculature, where sensor fluorescence predominantly comes from the phloem, and the epidermis were at least partly due to differences in sugar status. External supplementation with Suc induced a strong increase in the tS/mC ratio indicative of a reduction of the NAD pool (Figure 5C), implying that the Suc was taken up, imported into the cell, and metabolized. The

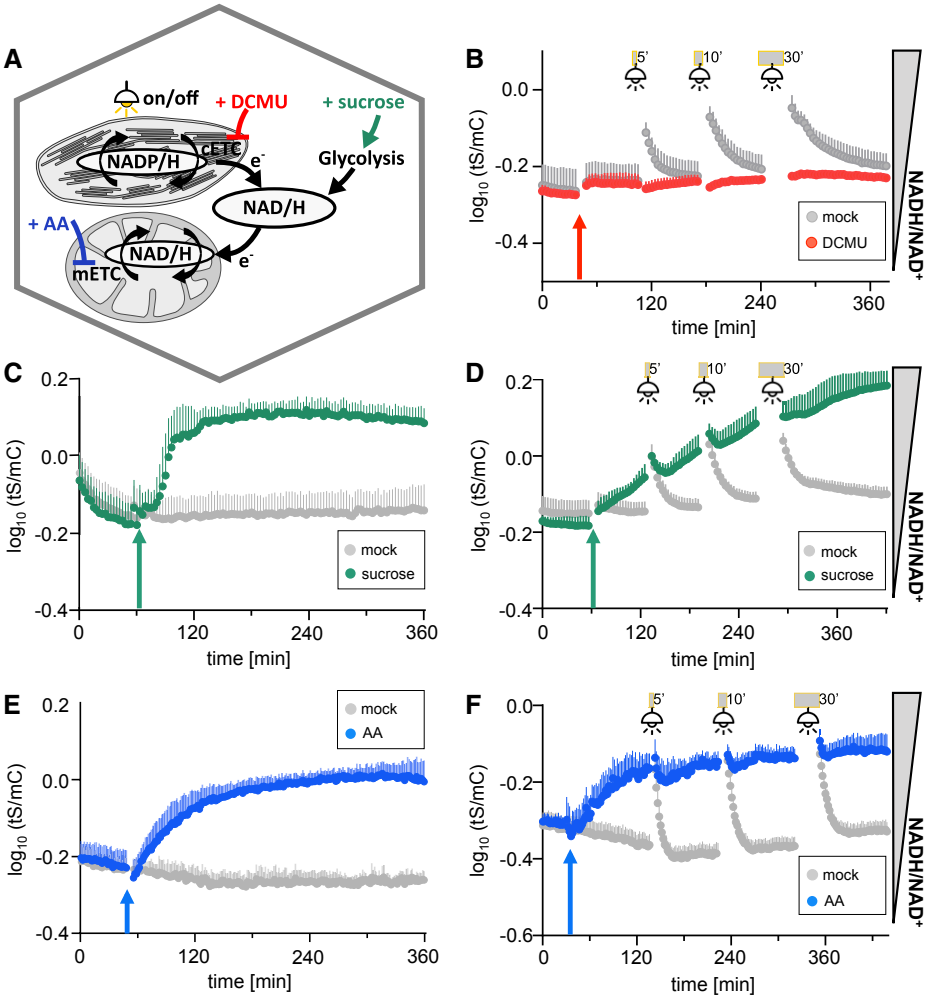

Figure 5. Dynamic Response of Cytosolic NAD Redox Status to Changes in Illumination, Respiratory Activity, and External Sugar Supply Using Multiwell Plate Reader–Based Fluorimetry.

(A) to **(F)** Overview of the stimuli used to explore cytosolic NAD redox dynamics: illumination to activate photosynthesis including the chloroplastic electron transport chain (cETC) and cETC inhibition with photosystem II inhibitor DCMU **(B)**, external Suc supplementation **(C)**, inhibition of the mETC at complex III by AA **(E)**, or combined stimuli (see **[D]** and **[F]**). Fluorescence emission was measured in each well, $\log_{10}$ transformed, and averaged sensor ratios were plotted after autofluorescence correction using Col-0 leaves.

(B) to **(F)** Time-course measurements of Peredox-mCherry ratio ($\log_{10}$(tS/mC)) of leaf discs from 5-week-old plants. Arrows indicate treatment and control treatment (mock) application after at least 90-min dark adaption. Excitation at 400 ± 10 nm (tS) and 570 ± 10 nm (mC), emission at 515 ± 7.5 nm (tS) and 610 ± 5 nm (mC). $n \geq 5$, means + SD.

(B) Addition of 10 μM DCMU (red arrow) and exposure to actinic light (400 μmol m^{-2} s^{-1}) for 5, 10, or 30 min (gray bars), respectively. Fluorescence emission was measured in each well every 200 s.

(C) Addition of 5% (w/v) Suc or assay medium as a mock control; cycle time of fluorescence emission measurement per well: 200 s.

(D) Combination of Suc treatment as in **(C)** with light exposure as in **(B)** with identical measurement cycle time.

(E) Addition of 20 μM AA or ethanol as a solvent control. Fluorescence emission was measured in each well every 94 s.

(F) Combination of AA treatment as in **(E)** with light exposure as in **(B)**. Fluorescence emission was measured in each well every 107 s. The experiments were repeated independently at least three times with consistent results.

reductive impact of Suc feeding on the cytosolic NAD pool, as demonstrated here for leaf discs, may be accounted for by a boost in glycolysis and the TCA cycle.

While photosynthetic activity and Suc feeding both boost the rate of reductant influx into the cytosolic NAD pool, we next tested the impact of decreasing the rate of reductant efflux by inhibiting mitochondrial electron transport as a major reductant sink. Inhibiting complex III using antimycin A (AA) led to the gradual reduction of NAD in the cytosol (Figure 5E). The observation that inhibiting mitochondrial function leads to pronounced responses in the cytosol supports the concept that cytosolic NAD redox state is dependent on mitochondrial electron transport activity, both directly via external NADH dehydrogenases and indirectly by metabolite shuttles (Heber, 1974; Fernie et al., 2004; Selinski and Scheibe, 2019).

Similar NAD redox responses to those observed in leaf discs were also observed in 5-d-old seedlings (Supplemental Figures 6A and 6B) and were reproducible between the different independent sensor lines (Supplemental Figure 6C), highlighting the robustness of the metabolic responses. The dynamics of the individual fluorescence signals of tS and mC further validate this technique. As expected from the sensor design concept, the mC signal remained largely stable over time, while tS was responsible for the transitions observed in the tS/mC ratio (Supplemental Figure 6D).

Combining light treatment with either Suc supplementation (Figure 5D) or inhibition of mitochondrial electron transport (Figure 5F) had a cumulative impact. Suc and AA induced gradual NAD reduction, which was only mildly increased further by illumination. Similarly, re-oxidation after illumination was abolished. Since this was the case at different stages of the gradual NAD reduction (Figure 5D), it is unlikely that the abolished re-oxidation was caused by sensor saturation.

The reversible responses to external stimuli are suggestive of a remarkable degree of physiological flexibility of the cytosolic NAD pool, which is now accessible for specific measurement. Exclusive cytosolic NAD redox monitoring after the application of organelle-targeted stimuli demonstrates efficient reductant exchange between the subcellular compartments, which is likely due to the tight association of NAD redox status to the metabolic network and mediated by active metabolite shuttle systems.

Engineering a Sensor Variant for Monitoring More Reduced NAD Pools

The pronounced responses of Peredox-mCherry indicate that it is well suited to cover the physiologically relevant range of NAD redox states in the cytosol. However, the responses in leaves covered a large proportion of the full spectroscopic dynamic range of the sensor, indicating that it is likely to reach saturation at its maximal amplitude. Furthermore, reductive responses in tissues with already more reduced NAD pools are expected to be limited by the sensitivity of the sensor. To address this limitation and to expand the range in which NAD redox measurements can be performed, we aimed to engineer a sensor variant with a lower binding affinity for NADH for measuring higher NADH/NAD^+ ratios (Figure 6). We chose a structure-informed rationale to destabilize NADH binding by replacing an Asp (D) with a Ser (S) in both Rex domains (Figure 6A). This D is conserved in NAD-dependent oxidoreductases (Laurino et al., 2016) and stabilizes NAD binding through hydrogen bonding with a hydroxyl-group of the NAD Rib moiety. To generate the "Peredox-mCherry DS" variant, we used targeted mutagenesis of the sensor sequence and expressed the sensor variant recombinantly to assess its biochemical properties.

The DS variant showed decreased binding affinity to NADH, with a K_d-value for NADH of 31.4 ± 4.4 μM compared to 1.2 ± 0.15 μM for Peredox-mCherry in the presence of 500 μM NAD^+ (Figure 6B; Supplemental Figure 7A). The K_d-value for NADPH (measured in the presence of 150 μM $NADP^+$) remained one order of magnitude higher at 324 ± 18 μM NADPH. The spectroscopic dynamic range (δ) was 2.88, that is, slightly higher than that of Peredox-mCherry (δ = 2.2). While the pH stability of the Peredox-mCherry sensor was maintained (Figure 6C), the NADH binding and NADH dissociation kinetics were accelerated in the DS variant. Following the rationale of assessing the kinetics of Peredox-mCherry (Figure 2E), we determined the binding kinetics of the DS variant at 500 μM NAD^+ and 30 μM NADH to ensure that both species bind to the sensor at a ratio of ~1:1. At NADH binding, tS/mC of the DS variant required 26.5 ± 4.5 s to increase to 50% of the full response amplitude (2.75 times faster than Peredox-mCherry at equivalent sensor occupation; Figure 6D). Replacement of NADH through the addition of NAD^+ (500 μM) took 1038 ± 217 s to reach 50% of the response amplitude (4.9 times slower than for Peredox-mCherry, one-phase decay fit; Supplemental Data Set 1H).

The decreased (albeit not absent) NAD^+ response of the NADH-bound DS variant in terms of both speed and impact on sensor ratio prompted us to assess the NAD^+ dependence of both Peredox-mCherry and Peredox-mCherry DS in further detail (Supplemental Figures 7B to 7E). Interestingly, these titrations revealed that NAD^+ concentration had a much more minor impact on the sensor response to NADH of the DS variant compared to Peredox-mCherry. The reduced NAD^+ sensitivity may be explained by the replacement of the negatively charged D by a neutral S at the binding pocket, by which charge-based stabilization of NAD^+ binding appears to be lost. As a result, the DS variant is mainly responsive to NADH concentration instead of NADH/NAD^+ ratio. Under physiologically meaningful conditions, where NAD^+ concentrations are stable compared to NADH, the increased K_d remains the dominant change in the DS variant compared to Peredox-mCherry. The decreased affinity of Peredox-mCherry DS is expected to allow more reduced NAD pools to be investigated compared to Peredox-mCherry, which can be critical depending on external conditions, tissue, and subcellular compartment. Specifically, with respect to the data presented here, we asked whether the DS variant may allow for discrimination between biological and technical causes when tS/mC ratio kinetics reach a plateau at high ratios (reduced NAD pool), as illustrated in Figures 5C and 5E.

Peredox-mCherry DS Expands the Response Range of in Vivo NAD Redox Sensing

To explore the response characteristics of the Peredox-mCherry DS variant, we generated Arabidopsis lines constitutively expressing Peredox-mCherry DS in the cytosol and nuclei

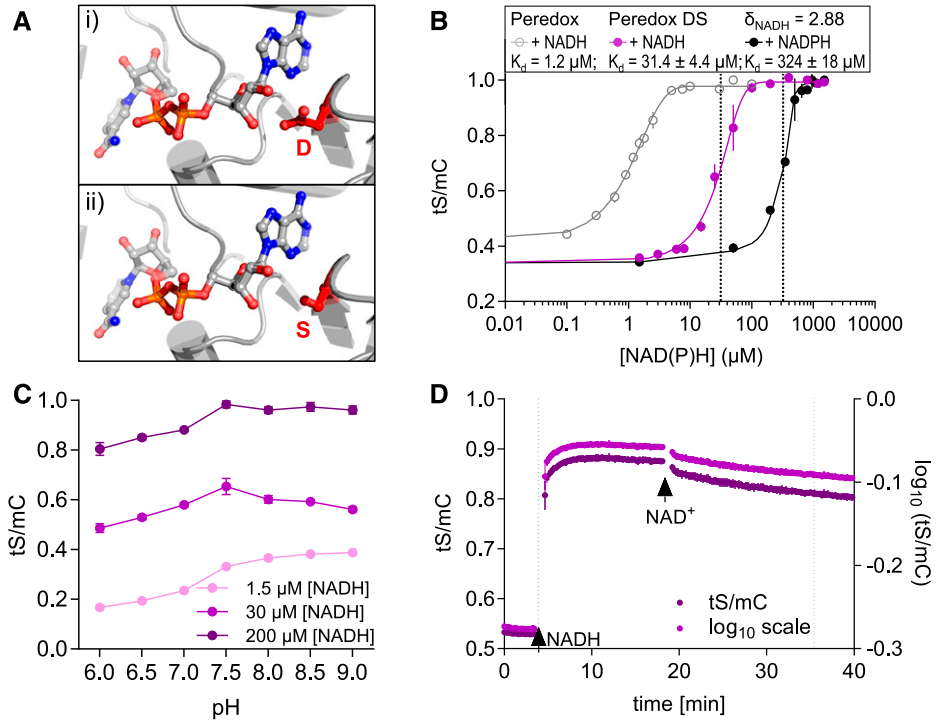

Figure 6. In Vitro Characteristics of the Peredox-mCherry DS Variant.

(A) Structural model of the Rex binding pocket for NAD(H) (PDB: 3IKT). (i) A D residue stabilizes NAD binding through a hydrogen bond with a Rib hydroxyl-moiety. (ii) This D was exchanged for an S to abolish the hydrogen bond and to decrease the binding affinity in the DS variant.

(B) Ratiometric response of the Peredox-mCherry DS variant compared to Peredox-mCherry (log_{10}(tS/mC)) at different NADH and NADPH concentrations in the presence of 500 µM NAD^+ and 150 µM $NADP^+$, respectively. Sensor protein concentration: 0.025 µg/µL, $n = 3$, mean ± SD, pH 7.5. The ratio values were normalized to the highest ratio (set to 1). Dotted lines indicate K_d-values (sigmoidal curve fitting with details provided in Supplemental Data Set 1G).

(C) Response of the DS sensor variant to different pH values. Sensor protein was equilibrated with three different NADH concentrations (1.5, 30, and 200 µM) in the presence of 500 µM NAD^+ to achieve low, mean, and high NADH occupancy at different pH values (6.0 to 9.0, $n = 3$, mean ± SD; Bis-Tris for pH 6.0 to 7.0 and Tris-HCl for pH 7.5 to 9.0).

(D) NADH binding to and dissociation from Peredox-mCherry DS in vitro. Time resolved tS/mC (magenta, left *y* axis) and corresponding log_{10} ratio (dark purple, right *y* axis) changes in recombinant sensor protein (0.025 µg/µL, Tris-HCl, pH 7.5) in response to NADH (30 µM, first arrow) in the presence of 500 µM NAD^+ and to further NAD^+ addition (500 µM, second arrow). Dotted lines indicate time to reach half of the response amplitude at NADH or NAD^+ addition (one-phase decay fit; Supplemental Data Set 1H). Fluorescence emission was measured every 13 s. Excitation, 400 ± 10 nm (tS) and 570 ± 10 nm (mC); emission, 520 ± 5 nm (tS) and 610 ± 5 nm (mC). The assay was independently repeated three times with consistent results.

(Supplemental Figures 8A to 8I). We selected three independent lines based on their bright fluorescence signal. Two-dimensional excitation–emission scans confirmed that the signals of tS and mC were sufficiently intense for measurements (Supplemental Figures 8J to 8L). All three sensor lines (#7 and #14 homozygous, #1 segregating) showed a wild-type–like phenotype (Supplemental Figure 8M). We then compared the responses of Arabidopsis leaf discs from 5-week-old plants expressing either Peredox-mCherry or Peredox-mCherry DS to illumination, the inhibition of respiration, and external Suc supplementation side by side by multiwell plate reader–based fluorimetry (Figure 7). Prior to any treatment, a significant difference in tS/mC steady state was consistently observed between tissues expressing the two sensor variants (Figure 7; Supplemental Figure 9A). A shift to lower ratios by the Peredox-mCherry DS variant could be expected due to the lower NADH affinity of the sensor (Figure 6B). The tS/mC ratio of Peredox-mCherry DS showed a diminished response to illumination (Figure 7A). With increasing light exposure times, a minor post-illumination reduction transient was observed. By contrast, inhibiting respiration with AA resulted in an increase in the tS/mC ratio of Peredox-mCherry DS, albeit at a lower rate than Peredox-mCherry (Figure 7B). As a result, the tS/mC values of DS variant only reached a plateau after 2.3 h, that is, 2.7-fold slower than Peredox-mCherry. This difference is in line with the higher K_d of the DS variant and suggests that the plateau reached by Peredox-mCherry represented saturation of the sensor rather than physiological stabilization of the NADH/NAD^+ ratio.

As an alternative approach to interfere with NADH oxidation by the mitochondria, we used low oxygen (2.5%) to induce hypoxia (Figure 7C; Wagner et al., 2019). At decreasing oxygen concentrations, the cytosolic NAD redox state, as monitored by Peredox-mCherry, rapidly shifted toward reduction. Once the oxygen concentration was stabilized at 2.5%, reduction progressed more slowly. Re-establishment of normoxia triggered the gradual re-oxidation of NAD. The response dynamics of Peredox-mCherry and Peredox-mCherry DS were very similar at the qualitative level,

but the relative tS/mC changes were less strong for DS, as expected since it has a lower K_d. Both sensors resolved the NAD redox response dynamics when NAD was shifted toward reduction, without sensor saturation. Comparing the impact of Suc supplementation on the in vivo responses of Peredox-mCherry (Figure 7D) and Peredox-mCherry DS (Figure 7E) further validated the characteristics of the DS variant. Suc induced a concentration-dependent increase in the tS/mC of both Peredox-mCherry and Peredox-mCherry DS, with a $\log_{10}$-response range of ~0.4 (δ of ~2.5) for both two sensor variants, covering their entire spectroscopic dynamic range. The rate of tS/mC increase was concentration dependent up to 10% (w/v) Suc. The plateau of saturated tS/mC values was reached by Peredox-mCherry after 11 h (1%), 2.7 h (5%), and 1.3 h (10%), and reaching the plateau took ~2.7 times longer for the DS variant (28.2 h for 1%, 7.5 h for 5%, 3.6 h for 10%, one-phase decay fit of ratio values from time point of treatment; Supplemental Data Set 1I).

Unexpectedly, we also observed a pronounced impact of elicitor exposure on cytosolic NAD redox dynamics (Figure 7F). Monitoring cytosolic NAD redox dynamics of leaf discs in response to the bacterial elicitor flg22 revealed a rapid and transient reduction, the timing of which appeared to correlate with stimulation of plant NADPH oxidase (respiratory burst oxidase homolog [RBOH]) activity (Nietzel et al., 2019). The characteristic and rapid dynamics allowed for a side-by-side comparison of Peredox-mCherry and the DS variant in vivo. Peredox-mCherry responded with an initial linear increase in $\log_{10}$(tS/mC) ratio of 0.51 $\pm$ 0.11 per hour, whereas the response rate by Peredox-mCherry DS was nearly twice as high (0.95 $\pm$ 0.31 per hour; Figure 7Fi). That is in line with the faster in vitro NADH binding rate of the DS variant. The amplitude of the DS variant was much lower than that of Peredox-mCherry (0.105 $\pm$ 0.011 versus 0.177 $\pm$ 0.034; Figure 7Fii), which is consistent with a lower affinity for NADH. Strikingly, the DS variant reached the maximum of the transient much earlier than Peredox-mCherry (18.6 $\pm$ 2.02 versus 41.38 $\pm$ 1.48 min; Figure 7Fiii), which probably results from a combination of the different binding and dissociation kinetics as well as the different affinities for NADH and the differential NAD^+ sensitivities. Redox responses were reproducible between the different independent DS sensor lines (Supplemental Figures 9B to 9D), highlighting the robustness of the metabolic responses. The similarity of the dynamics of Peredox-mCherry DS and Peredox-mCherry at the qualitative level (Figures 7A to 7E) validate faithful responses with the same in vivo specificity by both sensors.

DISCUSSION

Understanding in Vivo Metabolism Requires a Dynamic Understanding of NAD Redox Status

Monitoring intracellular NAD redox dynamics in planta has been a long-standing challenge. Established approaches to measure NADH and NAD^+ concentrations or NADH/NAD^+ ratios by performing enzymatic assays, analytical methods from whole-cell extracts, inference from marker metabolites, or in vivo using NAD(P)H autofluorescence are limited in their spatial or temporal resolution (Williamson et al., 1967; Queval and Noctor, 2007; Blacker et al., 2014). Analytical methods such as HPLC analysis can offer high accuracy and absolute quantitation, at the cost of mixing subcellular pools (Lu et al., 2018). An exception has been subcellular fractionation of pea leaf protoplasts (Igamberdiev and Gardeström, 2003), which indeed allowed subcellular NAD pools to be resolved and their changes measured in response to modified light and CO_2 supply. While this method remains technically challenging, which has prevented its broader adoption, the recent refinement of nonaqueous fractionation techniques may hold promise for performing analytical NAD measurements in nonprotoplast systems (Fürtauer et al., 2016; Beshir et al., 2019; Medeiros et al., 2019). Although rapid changes are an integral feature of plant metabolism, including redox metabolism (Eberhard et al., 2008), it has remained extremely challenging to capture NAD redox changes with a temporal resolution that matches these metabolic fluctuations. As a consequence, direct evidence remains scarce about how different cell compartments are differentially and dynamically affected by metabolic fluctuations as induced, for instance, by light-to-dark transitions. Recent NAD redox measurements in rapidly isolated mitochondria allowed absolute as well as relative NAD redox states to be determined, but rapid organelle isolation approaches cannot be analogously implemented for the cytosol (Luo et al., 2020). Furthermore, it is difficult to quantify the impact resulting from the organelle isolation procedure by removing organelles from the intact plant system. In vivo autofluorescence measurements of NADH and NADPH allow for temporal resolution but lack the specificity to distinguish NADH from NADPH. In addition, these measurements are technically challenging in plants due to interfering autofluorescence from other cellular compounds in the short wavelength range (Shaw and Ehrhardt, 2013). Yet, it is evident that an understanding of NAD redox dynamics, as they occur in the living plant at a tissue, cellular, and subcellular scales, will be critical if we are to integrate our mechanistic understanding about NAD biochemistry into a meaningful physiological framework in planta.

Peredox-mCherry Sensor Lines Allow NAD Redox Dynamics to Be Analyzed in the Plant Cytosol

The Arabidopsis sensor lines that we introduce here show constitutive cytosolic expression (Figure 1) and are not affected by silencing effects, as judged from the regular use of these lines for experimentation for up to 7 years. Unambiguous targeting and stable expression is in contrast to observations for several other sensors associated with severe silencing and subcellular mistargeting (Albrecht et al., 2011; Behera et al., 2015; Schwarzländer et al., 2016). Despite the successful expression in the plant cytosol and nucleoplasm, efforts to target Peredox-mCherry into mitochondria with three different constructs did not lead to the generation of any transformants, suggesting that the size (103.5 kD) and structure of the biosensor interfere with mitochondrial protein import, which leads to embryo lethality. This interpretation remains speculative but is consistent with the phenotypes of plants expressing other mitochondrial sensors (De Col et al., 2017; Nietzel et al., 2019). Peredox-mCherry is significantly larger than any of the sensors that we have found to cause phenotypes, and it contains two fluorescent protein domains, which may be able to arrest import if folding and/or chromophore maturation takes

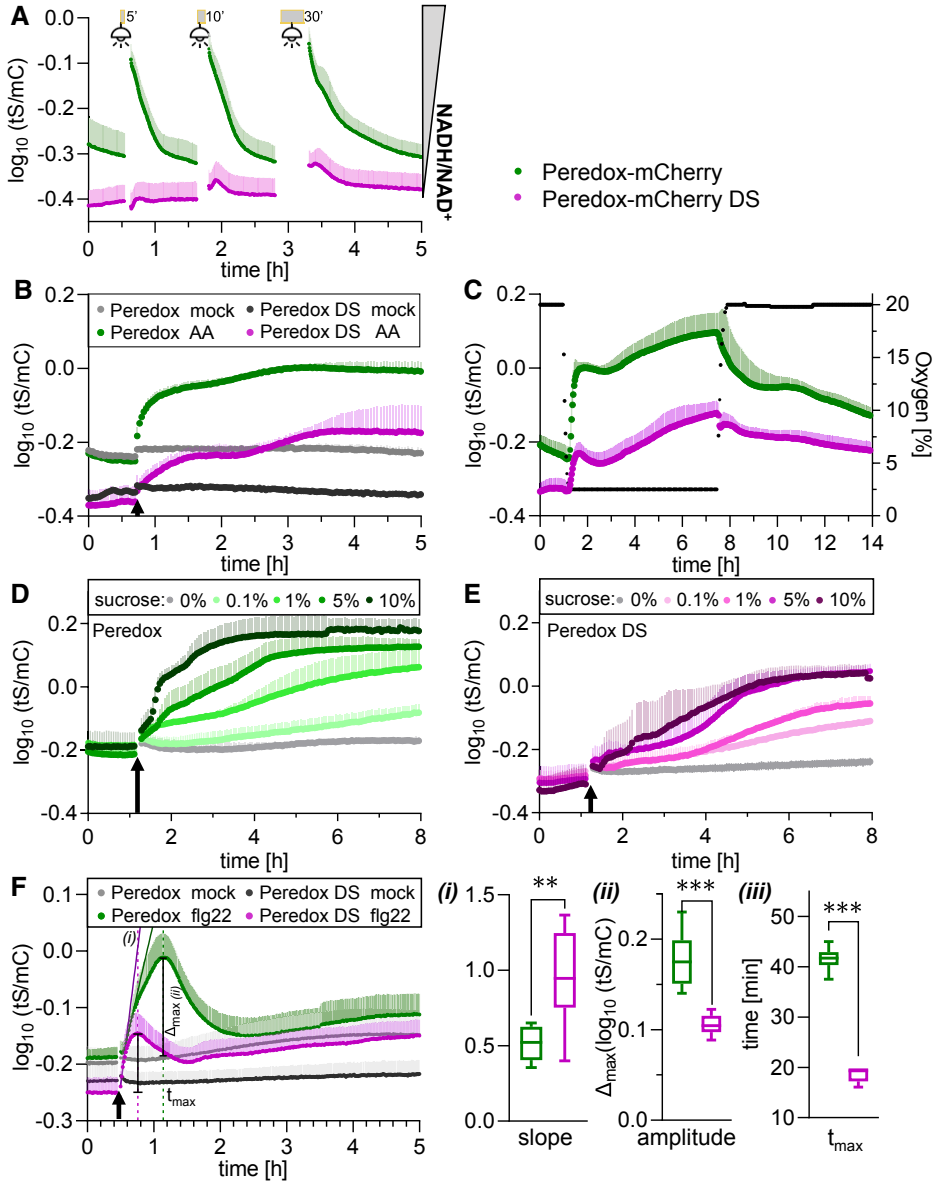

Figure 7. In Vivo Peredox-mCherry DS Response Range of NAD Redox Dynamics upon Changes in Illumination, Respiratory Activity, and External Sugar Supply.

Side-by-side multiwell plate reader–based time-course measurements of Peredox-mCherry and Peredox-mCherry DS ratio ($\log_{10}$(tS/mC)) of leaf discs from 5-week-old Arabidopsis plants dark adapted for at least 90 min prior to treatments. Excitation at 400 ± 10 nm (tS) and 570 ± 10 nm (mC); emission at 515 ± 7.5 nm (tS) and 610 ± 5 nm (mC). $n \geq 5$, means + SD.

(A) Exposure to actinic light (400 μmol m^{-2} s^{-1}) for 5, 10, or 30 min (gray bars). Fluorescence emission was recorded every 25 s in each well.

(B) Addition of 20 μM AA or ethanol as a solvent control (mock). Arrows indicate treatment application. Cycle time of fluorescence emission measurement per well: 120 s.

(C) Hypoxia induction by lowering the oxygen concentration to 2.5% by substitution of air with nitrogen. Green dots, Peredox-mCherry; purple dots, Peredox-mCherry DS; black dots, oxygen concentration. Oxygen concentration is indicated by the right *y* axis; cycle time of fluorescence emission measurement per well: 120 s.

(D) and **(E)** Supplementation with different Suc concentrations (0 to 10% [w/v] in assay medium) at the indicated time point (arrow) for Peredox-mCherry **(D)** and Peredox-mCherry DS **(E)**. Fluorescence emission was recorded every 200 s in each well.

(F) Treatment with 10 μM flg22 (in assay medium) at the indicated time point (arrow) for Peredox-mCherry and Peredox-mCherry DS. (i) Slope of the linear regression during the linear increase of the transient in $\log_{10}$(tS/mC) per hour (Supplemental Data Set 1J). (ii) Transient amplitude (Δ_{max}). (iii) Time after treatment needed to reach the transient maximum (t_{max}). Student's *t*-test, $^{**}P < 0.01$, $^{***}P < 0.001$ (Supplemental Data Set 1J). Measurements were repeated independently at least three times with consistent results.

place before import is completed. Importantly, expression of Peredox-mCherry in the plant cytosol did not induce growth phenotypes (Figure 1). This is consistent with the idea that NAD binding to the sensor in addition to the many endogenous NAD binding proteins does not disrupt cytosolic NAD physiology.

Biochemical Characteristics of Peredox-mCherry Fit Plant Cytosolic Physiology

We selected Peredox-mCherry over other NAD biosensors, as it is the only sensor that reports changes in the NAD redox status rather than changes in NADH or NAD^+ concentration, while providing a ratiometric readout and being largely pH inert (Figure 2; Hung et al., 2011). In vivo, the NAD redox state is predominantly set by the activity of the metabolic oxidoreductases, some of which can carry large fluxes and use NAD as a cofactor. De novo NAD^+ synthesis, subcellular transport, recycling through the salvage pathway, degradation and utilization as a substrate, and the conversion of NAD(H) to NADP(H) by NAD(H) kinases (and vice versa by phosphatases) are generally less rapid and are expected to have a much smaller impact on NAD redox status. Instead, they can adjust subcellular NAD pool size (Noctor et al., 2006; Kawai and Murata, 2008; Waller et al., 2010). As such, it is the NADH/NAD^+ ratio, as opposed to the concentrations of NADH or NAD^+, that is the decisive parameter to measure when exploring dynamics in redox metabolism. Since both NADH and NAD^+ bind to Peredox-mCherry and Peredox-mCherry DS, but only NADH binding affects tS fluorescence, both sensors report NADH/NAD^+ ratios, while changes in total NAD^+ and NADH concentrations cannot be monitored (Hung et al., 2011).

Previous estimations based on rapid subcellular fractionation of pea leaf protoplasts indicated an NADH/NAD^+ ratio between 0.03 to 0.2, with NAD^+ at ~500 μM and NADH at ~20 μM (Igamberdiev and Gardeström, 2003). Considering the difference in concentration between both NAD species, any ratio change by NAD^+-NADH interconversion will be dominated by the change in NADH concentration, while NAD^+ concentration will have only a minor influence. Moreover, the sensor provides a readout only for the free NAD pool, which remains largely unchanged regardless of the content of NAD bound to proteins (Kasimova et al., 2006). A substantial fraction of the total NAD pool was estimated to be bound to proteins in plant mitochondria (e.g., 30 to 50% of NAD^+ and 75% of NADH; Kasimova et al., 2006), similar to mammalian erythrocytes (50% free NAD; Canepa et al., 1991). Although the NAD redox state is independent of total NAD pool size (in contrast to, e.g., glutathione), preferential sequestration or release of NAD^+ or NADH between the bound and free NAD pools may still lead to considerable redox changes of the free pool. Combinatorial analyses with sensors that monitor NAD^+ concentration (Cambronne et al., 2016) have the potential to further uncover the interplay between in vivo NAD pool sizes and redox status in the future.

An important characteristic of Peredox-mCherry is the overall stability of its readout under physiological pH changes (Figure 2). The impact of pH changes on the response of fluorescent biosensors remains a widespread problem that has previously led to ambiguous interpretations (Schwarzländer et al., 2011, 2012, 2014). The issue is increasingly recognized and has stimulated the development of pH-stable sensor variants and dedicated correction protocols (Tao et al., 2017; Nietzel et al., 2019; Pak et al., 2020). Also, the development of Peredox-mCherry included a dedicated mutagenesis and screening step to identify a pH inert sensor (Hung et al., 2011), while alternative sensors for NAD redox dynamics, such as SoNar, show pronounced pH dependence (Zhao et al., 2015). pH stability is particularly relevant for the use of sensors in plants under conditions known to trigger intracellular pH changes, such as hypoxia, under which cytosolic pH can drop by more than 1 pH unit (Geigenberger, 2003; Wagner et al., 2019). However, pH changes are also relevant under nonstress conditions and require careful consideration. Physiological events, such as Ca^{2+} transients or change in illumination status, can trigger pH changes in the range of 0.1 to 0.5 units (Yin et al., 1990; Mühling et al., 1995; Behera et al., 2018), which bears a considerable risk of generating pH-related sensing artifacts when pH-responsive biosensor variants are applied without caution and robust controls. Although cytosolic pH changes are highly likely to occur in response to the illumination, low oxygen, and respiratory inhibition treatments applied here, these changes are unlikely to have a pronounced impact of the response of the Peredox-mCherry sensors.

Toward an Integrated Understanding of Tissue-Specific NAD Redox Metabolism

Direct in vivo mapping of the cytosolic NAD redox state across an entire Arabidopsis seedling by confocal microscopy resolved a remarkable degree of heterogeneity between different tissues and cells (Figure 4). Green tissues showed more oxidized NAD redox states compared to heterotrophic tissues with more reduced NAD redox states. Since the seedlings were dark adapted before imaging, the more oxidized NAD pool in photosynthetically active tissues may reflect its capacity to accept electrons exported by the chloroplast in the light, and indeed illumination of leaf discs led to NAD pool reduction in the cytosol (Figure 5B; Figure 7A). Interestingly, the shoot-to-root redox gradient was markedly decreased in etiolated seedlings grown in the dark, mainly due to a more oxidized NAD pool in the root tissues (Figure 4). This suggests that photo-morphogenesis affects the redox metabolism of heterotrophic root tissues in particular. Superimposing the NAD redox seedling atlas with a recently reported cytosolic $MgATP^{2-}$ map (De Col et al., 2017) revealed a correlation between ATP concentration and NAD oxidation, which were generally both high in shoot tissues and both low in root tissues. Also, the shoot–root gradients of both ATP and NAD redox state were flattened in etiolated seedlings, raising the possibility that the correlation is underpinned mechanistically by metabolism, most likely respiration. This overall correlation was not observed in the SAM region, which displayed both low ATP levels and a particularly oxidized NAD pool. Low ATP levels are consistent with respiratory inhibition resulting from a hypoxic environment, which was recently found to regulate the development of leaf primordia (Weits et al., 2019). However, hypoxia is typically associated with NAD reduction, rather than oxidation (Figure 7; Chance et al., 1962; Wagner et al., 2019), raising intriguing questions about the specific metabolic programs used by cells in the meristem and leaf primordia.

Furthermore, cytosolic NAD generally appeared to be more oxidized in the vasculature than in the surrounding tissues. The sensor fluorescence signal in the vasculature most likely originates mainly from the phloem, which shows elevated Suc levels, high rates of oxygen consumption, and few intercellular air spaces and is prone to hypoxia (van Dongen et al., 2003). Like the shoot meristem region, a particularly reduced rather than oxidized NAD pool may be expected in the vasculature, considering that both increased Suc supply and hypoxia induced NAD reduction in leaf discs (Figures 5 and 7; Zhang et al., 2017). The possibility of a highly specialized phloem metabolism deserves further attention in the future, aided by sensor expression under cell type–specific promoters, such as the *SUCROSE-PROTON SYMPORTER2* promoter for phloem companion cells, in analogy to recent advances in cell type–specific transcriptome analyses and even organelle isolations (Boussardon et al., 2020; Rich-Griffin et al., 2020).

Cytosolic NAD Redox Dynamics Are Remarkably Flexible and Integrate Organelle Redox Metabolism

In addition to the dependence of NAD redox status on developmental status, online sensor monitoring revealed remarkable flexibility of the cytosolic NAD redox state, as apparent from the study of dynamic NAD redox responses in leaf tissue (Figures 5 and 7). While large fluctuations, rather than strict buffering, may seem counterintuitive for a central hub of the metabolic network, changes in cytosolic NADH/NAD^+ ratio are in general agreement with the results of previous analytical single time point measurements, for example, under different light and CO_2 conditions (Igamberdiev and Gardeström, 2003).

The reduction of cytosolic NAD in response to external Suc (Figures 5C, 7, and 7E) is in line with the efficient uptake of Suc into the cytosol and its breakdown by glycolysis and the mitochondrial TCA cycle, which is connected to the cytosol by metabolite shuttles. Even though the rate of NADH production likely increases in response to external Suc, the reduction of the NAD pool results from a shift in the balance between the rates of NADH production and NADH oxidation, suggesting that mitochondrial electron transport is unable to fully compensate for the increased flux through primary metabolism. This interpretation is validated by the increased NADH/NAD^+ ratio when mitochondrial electron transport capacity is constrained, as is the case under AA inhibition or hypoxia (Figure 5E, 7B, and 7C). The cytosolic response further emphasizes the notion that the mETC acts as major electron sink for cytosolic NADH, and the activity of metabolite shuttles and the external NADH dehydrogenases represent obvious links (Geigenberger, 2003; Rasmusson et al., 2004).

The responses of the sensors to illumination and respiratory inhibition provide direct in vivo evidence that the cytosol is central to integrating redox metabolism from the organelles. Since the in vivo measurements integrate all operational crosstalk mechanisms—known and unknown—and consider their relative quantitative contributions, these observations not only validate the wealth of previous biochemical measurements but also allow comparative measurements in response to different and combined external stimuli (Figures 5 and 7).

The activation of photosynthesis by illumination leads to a reduction of the cytosolic NAD pool, as indicated by the return of the sensor ratio to steady state in the dark (Figures 5B and 7A). The export of photosynthetic reductant from the chloroplast via the chloroplastic malate valve and triose phosphate-3-phosphoglycerate shuttle has been studied intensely and can prevent the photoinhibition of photosynthetic electron transport during illumination (Heber, 1974; Taniguchi and Miyake, 2012; Selinski and Scheibe, 2019; Shameer et al., 2019). Efficient electron shuttling through the malate valve depends on malate–oxaloacetate exchange across the chloroplast inner envelope, the light/thioredoxin-activated plastidic NADP-MDH, and cytosolic NAD-MDH (Wolosiuk et al., 1977; Scheibe and Jacquot, 1983; Hatch et al., 1984; Kinoshita et al., 2011). As such, the exported reductant from the NADP pool in the chloroplast stroma can enter the NAD pool in the cytosol, emphasizing the need to monitor cytosolic NAD rather than NADP in the context of photosynthetic redox metabolism. It should be emphasized, however, that the sensor response indicates net changes in NAD redox status, while the underlying gross electron flux rates cannot be resolved. It would be desirable to investigate NAD and NADP redox dynamics simultaneously in the future. A family of NADPH sensors was recently introduced, but caution should be taken before applying these sensors to studying plant NADPH dynamics and photosynthesis due to their pronounced inherent pH sensitivity (Tao et al., 2017).

While this work was under revision, Lim et al. (2020) reported the use of the NAD redox sensor SoNar and the NADPH sensor family iNap to assess the subcellular responses of redox metabolism to photosynthetic activity in the cytosol, chloroplast stroma, and peroxisomes of Arabidopsis cotyledons. The authors performed pH correction using control sensor constructs without pyrimidine nucleotide binding capacity expressed in separate control plants measured in separate experiments. Consistent with our observations based on Peredox-mCherry, the SoNar sensor lines did not show any obvious developmental phenotypes, and the measurements using the cytosolic SoNar sensor indicated a more oxidized NAD pool in roots than in shoots, as well as pronounced NAD pool reduction in response to mitochondrial electron transport inhibitors, such as AA. While the pH-corrected SoNar data indicated strong and reversible reduction of the stromal NAD pool in response to illumination, cytosolic NAD reduction was detectable, but the sensor response was subtle at light intensities that were only slightly lower than those applied here (296 versus 400 $\mu mol\ m^{-2}\ s^{-1}$). This apparent difference may be due to the different NAD binding and NAD response characteristics between Peredox-mCherry and SoNar, the required pH correction regime for SoNar, the difference in light intensity, and/or the use of cotyledons by Lim et al. (2020) compared to the true leaf tissue of 5-week-old Arabidopsis rosettes investigated here.

The mechanisms that underpin photosynthetic metabolism and redox dynamics between cell compartments likely differ between cotyledons and true leaves. The cumulative effects of illumination and respiratory inhibition clearly demonstrate that redox crosstalk between chloroplasts and mitochondria is integrated by the cytosolic NAD pool in true leaf tissue from 5-week-old rosettes (Figure 5F). This system provides a platform to experimentally dissect the relative significance of major processes in organelle energy metabolism and their impact on inter-organelle redox crosstalk, including that of cyclic electron flow, the photorespiratory pathway (as initiated by Lim et al. [2020] using

a pharmacological approach), and the alternative respiratory pathway. We have initiated reverse genetic approaches to manipulate chloroplast–cytosol–mitochondria interactions at various steps of metabolism and transport and expect online NAD redox monitoring to provide novel insight into their operation under changing external conditions in the future.

While the observed NAD redox dynamics in response to Suc, respiratory inhibition, hypoxia, and illumination (Figures 5 and 7) validate established mechanisms of intracellular redox metabolism, the observation of an elicitor-induced NAD redox transient came as a surprise and currently lacks a defined mechanistic foundation (Figure 7F). Since the transient is reminiscent of Ca^{2+} and reactive oxygen species transients that have been extensively investigated in the context of elicitor-induced NADPH oxidase/RBOH activity, the mechanism of NAD reduction may be directly or indirectly linked to RBOH activity as well. Recent work has implicated a calmodulin/Ca^{2+}-dependent NAD kinase in providing $NADP^+$ to support RBOH activity (Dell'Aglio et al., 2019). The phosphorylation of large amounts of NAD^+ at a high rate may indeed result in a reductive shift of the cytosolic NAD pool, even though any quantitative estimation of the actual impact remains highly speculative. Consistently, a knockdown mutant impaired in the first step of de novo NAD biosynthesis shows deficient flg22-triggered ROS production by RBOHD and reduced stomatal immunity (Macho et al., 2012). Reduction of the NAD pool by NAD^+ depletion may further be due to the elicitor-induced NADase activity of the Toll/interleukin-1 receptor homology (TIR) domains of TNL proteins, which degrade NAD^+ as an essential step in signaling between TNLs and ENHANCED DISEASE SUSCEPTIBILITY1 (EDS1; Wiermer et al. 2005; Wagner et al. 2013) to induce cell death (Horsefield et al. 2019; Wan et al. 2019). Moreover, a recent study established a link between impaired NAD biosynthesis and abscisic acid sensitivity, as mediated by SnRK2 protein kinases, RBOHF, and increased rates of reactive oxygen species production (Hong et al., 2020); high NADH/NAD^+ ratios in an NAD biosynthesis mutant caused increased RBOHF activity. Similarly, we observed a reduction of the NAD pool in response to the flg22-induced RBOHD/F-mediated respiratory burst (Kadota et al., 2014). In line with these results, defense-induced RBOHF activity has been implicated in pronounced metabolomic changes (Chaouch et al., 2012). Exactly how changes in NAD redox state and RBOH activity are mechanistically linked deserves further attention.

Peredox-mCherry DS Variant Expands the Measurement Range for NAD Redox Dynamics

The pronounced flexibility of NAD redox dynamics poses the challenge that a single sensor variant cannot cover the full spectrum of physiological responses. By performing structure-informed targeted mutagenesis, we generated a Peredox-mCherry DS variant that is able to resolve a higher NADH concentration range while showing decreased NAD^+ binding (Figure 6; Supplemental Figure 7). Even though the DS variant indicates NADH concentration rather than NADH/NAD^+, the physiological responses of both sensors can be compared, and the DS variant reports NAD redox in vivo under the assumption that changes in NAD^+ are minor compared with changes in NADH (which is justified in the cytosol under physiological conditions). When starting from a comparatively oxidized NAD pool, as the case in Arabidopsis leaves, the response to NAD reduction was slower for the DS variant compared to Peredox-mCherry, while the tS/mC values of the DS variant continued to increase in the presence of a more reduced NAD pool, when those of Peredox-mCherry have already reached saturation (Figures 7B to 7E). This behavior is in line with the lower NADH binding affinity of the DS variant, as observed in vitro (Figure 6B). On the other hand, the DS variant responded to elicitor exposure at a higher rate than Peredox-mCherry, indicating that in the initial phase of the rapid transient, its faster NADH binding kinetics appear to dominate the response rate (Figure 7F). As Peredox-mCherry can reach saturation under conditions that are physiologically meaningful in the plant cytosol (Figures 4 and 5), the DS variant is able to respond to more reduced NAD redox states. Conversely, Peredox-mCherry DS is limited in resolving the dynamics of more oxidized NAD redox states, as indicated by the light response (Figure 7A) and the lower amplitude of the flg22-induced transient (Figure 7F), suggesting that the DS variant is fully devoid of bound NADH in the dark. As a result, the combination of both sensors expands the range of NAD redox dynamics than can be resolved, and their respective use can be matched to the expected NAD redox dynamics of the specific physiological scenario to be investigated. If the problem of mitochondrial targeting can be resolved in the future, the DS variant might be a good candidate to monitor NAD redox dynamics in mitochondria, which are estimated to display 100- to 1000-fold higher NADH/NAD^+ ratios than the cytosol (Williamson et al., 1967; Igamberdiev and Gardeström, 2003; Hung et al., 2011; Luo et al., 2020).

In principle, in vivo monitoring using two sensors with different affinities and their side-by-side calibration by driving the in situ NAD redox states to their extremes would allow spectroscopic sensor ratios to be converted to absolute NADH/NAD^+ ratios (and NADH concentrations) and NAD redox potential, as implemented, for example, for Ca^{2+} and glutathione redox sensing (Palmer and Tsien, 2006; Schwarzländer et al., 2008; Aller et al., 2013). However, any absolute quantitation of fluorescent protein sensor data should be interpreted with the utmost caution, since the conversion requires additional assumptions that are prone to error, resulting in the misleading representation of sensor data. Nevertheless, with this in mind, plausible estimates can be made. Previous estimations based on rapid subcellular fractionation of pea leaf protoplasts have indicated an NADH/NAD^+ ratio between 0.03 to 0.1, with NAD^+ at ~500 μM and NADH at ~20 μM (Igamberdiev and Gardeström, 2003); similar NADH/NAD^+ ratios were obtained from cellular extracts of cucumber (*Cucumis sativus*) leaves (Szal et al., 2008). Ratios of ~0.001, that is, at least one order of magnitude lower, are regularly determined in the cytosol of mammalian tissues (Williamson et al., 1967), suggesting that plants and mammals maintain a fundamentally different cytosolic NAD redox status or that the measurements in subcellular extracts still overestimate even lower in vivo ratios. The finding that Peredox-mCherry (K_d for NADH of 1.2 μM in the presence of 500 μM NAD^+, with a resulting K_{ratio} of 0.0024) responds to in vivo NAD reduction in the Arabidopsis cytosol, rather than being saturated, strongly suggests that NADH/NAD^+ ratios are in the order of 0.001, that is, similar to those determined in the mammalian cytosol. Assuming that cytosolic NAD^+ concentrations

from subcellular fractionation of pea leaf protoplasts (570 ± 30 μM in the dark; Igamberdiev and Gardeström, 2003) are also a good approximation for the Arabidopsis leaf (mesophyll) cytosol, free NADH concentrations of ~0.5 to 1 μM are estimated at steady state in the dark based on the biosensors (Figures 6 and 7), as opposed to 18 ± 14 μM NADH in cytosolic fractions from pea mesophyll protoplasts in the dark. These lower NADH values are consistent with other determinations from plant cell extracts, although these analyses lacked subcellular resolution (Heineke et al., 1991; Wigge et al., 1993).

Future Perspectives for NAD Redox Sensing in Plants

This work explored in vivo NAD redox dynamics in Arabidopsis. We carefully established an approach using a NAD sensor and showcased the power of this approach for plant research, while clearly just scratching the surface of its full potential. The ability to monitor NAD redox dynamics live and in cells of the intact living organism opens a methodological door to answering several long-standing and pressing questions. For instance, insights into the relationship between cellular redox metabolism and developmental programs will be in reach (de Souza Chaves et al., 2019; Feitosa-Araujo et al., 2020). Furthermore, the spatiotemporal signatures of NAD redox dynamics will shed light on the role of NAD under stress conditions or during immune responses (Zhang and Mou, 2009; Hashida et al., 2010; Pétriacq et al., 2012, 2016; Horsefield et al., 2019; Wan et al., 2019). Well-established concepts can also be put to the test in vivo, including the significance of alternative respiratory activity for subcellular redox metabolism (Michalecka et al., 2003; Rasmusson et al., 2008) or the differential roles of different metabolic redox shuttle systems (Selinski and Scheibe, 2019; Shameer et al., 2019). Biosensor expression driven by cell type–specific promoters will facilitate the analysis of cell type–specific metabolic modes and refine the NAD redox atlas generated here by global sensor expression. A particularly attractive route will be to obtain a systems perspective that links metabolic heterogeneity and plant development by integrating the cell-specific NAD redox data with data from other biosensors (e.g., for ATP or plant hormone distribution; Brunoud et al., 2012; Jones et al., 2014; Waadt et al., 2014; De Col et al., 2017; Rizza et al., 2017), but also with cell-specific microgenomic data, as well as single cell proteome and metabolite profiles once they become available (Bailey-Serres, 2013; Li et al., 2016). Finally, the optimization of NAD sensing for the apoplast, that is, the generation of high-affinity sensor variants that remain usable at very low pH, will open new avenues to understand the physiological context of extracellular NAD signaling (Wang et al., 2017, 2019).

METHODS

Generation of Expression Constructs and Plant Lines

The coding sequence of Peredox-mCherry was PCR amplified from GW1-Peredox-mCherry (Hung et al., 2011), inserted into pDONR207 (Invitrogen), and transferred to pSS02 (derivative of pMDC32; Curtis and Grossniklaus, 2003) as well as pETG10A by Gateway cloning (Invitrogen). pSS02 allows for the constitutive expression of genes in plants under the control of the *UBIQUITIN10* promoter; pETG10A allows for inducible expression of recombinant protein in *Escherichia coli* cells. The plasmid GW1-Peredox-mCherry (Hung et al., 2011) was obtained from Addgene (plasmid no. 32380; http://www.addgene.org/32380/). The DS variant was generated by site-directed mutagenesis. Primers used to change the two codons are listed in the Supplemental Table. Agrobacterium (*Agrobacterium tumefaciens*)–mediated transformation of Arabidopsis (*Arabidopsis thaliana*; accession Col-0) was performed by the floral dip method (Clough and Bent, 1998). Transformants and homozygous lines were selected based on the resistance marker for hygromycin and sensor fluorescence.

Plant Culture and Phenotyping

Arabidopsis seedlings were grown from surface-sterilized seeds on vertical plates containing half-strength Murashige and Skoog (MS) medium (Murashige and Skoog, 1962) with 10 mM 2-(*N*-morpholino)ethanesulfonic acid (MES buffer), pH 5.8 (KOH), supplemented with 1% (w/v) Suc and 1% (w/v) agar and cultivated under long-day conditions (16 h, 75 to 100 μmol photons $m^{-2} s^{-1}$ using Osram L 18W 840 Lumilux cool-white or Philips TL5 HO 49W 840 [MASTER] cool-white tubes at 22°C, 8 h dark at 18°C) after stratification for 2 d at 4°C in the dark. Primary root length was documented from seedlings growing side by side with their corresponding controls and measured using ImageJ ($n = 25$). To analyze leaf rosette development and measure primary inflorescence height, plants were individually transferred to soil after 5 d and regularly documented photographically. Leaf rosette size was analyzed using the custom Leaf Lab tool (version 1.41) as previously described by Wagner et al. (2015), and height of the primary inflorescence was quantified using ImageJ ($n = 19$ to 20). To prepare leaf discs, plants were germinated and grown in soil under long-day conditions.

Purification of Recombinant Sensor Proteins

Protein expression and purification were performed according to De Col et al. (2017) with the following modifications: *E. coli* strain BL21 (DE3) ArcticExpress cells carrying pETG10A:Peredox-mCherry or pETG10A:-Peredox-mCherry DS were selected for overexpression based on an optimization assay (Supplemental Figure 2). Overexpression was induced by isopropyl β-D-1-thiogalactopyranoside at a final concentration of 0.1 mM. Cells were collected by centrifugation at 5000*g* for 15 min at 4°C, and the pellet was resuspended in Tris buffer (50 mM Tris-HCl, pH 7.5, 100 mM NaCl, and 0.5 mM $MgCl_2$) supplemented with 1 mg/mL lysozyme, 0.1 mg/mL DNaseI (Roche), and complete protease inhibitor cocktail (Roche). After a 30-min incubation on ice, the cells were sonicated (3 × 2 min, 50% power output, 50% duty cycle). The lysate was centrifuged at 40,000*g* for 30 min at 4°C, and the supernatant was loaded onto a Ni^{2+} nitrilotriacetic acid HisTrap column (GE Healthcare). Proteins were eluted with an imidazole gradient (10 to 250 mM in Tris buffer) using an ÄKTAprime plus system (GE Healthcare). Fractions containing recombinant protein were pooled, concentrated by ultrafiltration, and applied to a HiLoad 16/600 Superdex 200 column (GE Healthcare) pre-equilibrated with Tris buffer. Concentrated Peredox-mCherry and Peredox-mCherry DS supplemented with 20% (v/v) glycerol were stored at –80°C.

Characterization of Sensor Protein in Vitro

The concentration of purified recombinant sensor protein was quantified according to Bradford (1976). Protein at a final concentration of 0.25 μM was mixed with Tris buffer for all in vitro assays, except for the pH assays, in which Tris was replaced by Bis-Tris for pH 6.0 to 7.0. An FP-8300 spectrofluorometer (Jasco) was used at 25°C to excite tS at 400 ± 5 nm with emission spectra recorded between 450 and 600 ± 5 nm and to excite mC at 580 ± 5 nm with emission spectra recorded between 600 and 650 ± 5 nm (Supplemental Figure 3). tS/mC ratios were calculated from the

fluorescence maxima empirically determined at 513 and 604 nm, respectively, after NAD(P)H autofluorescence correction (Supplemental Figure 3C). Sensor proteins were allowed to equilibrate with 500 μM NAD^+ (or 150 μM $NADP^+$) for 30 min prior to measurements to ensure that no residual NADH was bound to the sensor. To compare the ratiometric responses of sensor proteins to NADH versus NADPH in the presence of 500 μM NAD^+ and 150 μM $NADP^+$, respectively, ratio values were normalized to the highest ratio (set to 1). K_d-values were determined by sigmoidal curve fitting using Prism software (version 8.0.1; GraphPad).

Isolation of Mitochondria

Mitochondria were isolated from the 16-d-old wild-type Arabidopsis seedlings grown in hydroponic pots under long-day conditions as described previously by Sweetlove et al. (2007) and Schwarzländer et al. (2011).

Multiwell Plate Reader–Based Fluorimetry

tS and mC were excited at 400 ± 5 and 540 ± 10 nm, respectively, and emission was collected at 520 ± 5 and 615 ± 9 nm in a CLARIOstar microplate reader (BMG Labtech). For in vivo experiments with Arabidopsis leaf discs or seedlings, samples were monitored in a total volume of 200 μL of assay medium (10 mM MES, 5 mM KCl, 10 mM $MgCl_2$, and 10 mM $CaCl_2$, pH 5.8) using top optics with adjusted focal height to 6 to 8 mm, 25°C incubation temperature, well-multichromatic monitoring, and 40 flashes per well and measuring cycle with orbital averaging to minimize local fluorescence artifacts. Sample sizes represent total number of leaf discs, which were cut from three to eight different plants per line cultured side by side under the same conditions. A maximum of 12 leaf discs per plant were cut and equally distributed to the treatment and mock control groups. Experiments were independently repeated with three different sensor lines and different plant batches of the same sensor line to validate the reproducibility of the results and to justify the presentation of representative data sets. Plates were kept in the dark for at least 90 min before recording to minimize potential effects of active photosynthesis. For the dark–light–dark transition experiments, measurements were paused, the plates were moved to be illuminated from the top (400 μmol s^{-1} m^{-2}) for 5, 10, or 30 min, respectively, after which measurements were continued. For in vitro monitoring of mitochondrial NADH oxidation, assays were adapted from De Col et al. (2017). Proteins (10 μg) from freshly isolated mitochondria were supplemented with 500 μM NAD^+ and 0.5 μM purified recombinant Peredox-mCherry in a total volume of 200 μL per well. Samples were imaged using top optics with a focal height of 8.0 mm, 50 flashes per well and measuring cycle (orbital averaging), and double orbital shaking at 400 rpm for 10 s before each measurement cycle (excitation at 400 ± 10 and 570 ± 10 nm, emission collected at 515 ± 7.5 and 610 ± 5 nm, respectively, for tS and mC).

Confocal Laser Scanning Microscopy

Confocal imaging of 5-d-old Arabidopsis seedlings was performed using a DMi8 inverted microscope equipped with a TCS SP8 laser scanning device (Leica Microsystems) and a ×10 (0.40 numerical aperture) or ×40 (1.10 numerical aperture, water immersion) lens as previously described by Wagner et al. (2015). tS fluorescence excited at 405 nm was recorded at 517.5 ± 7.5 nm and mC fluorescence excited at 575 nm (White Light Laser at 85%) was recorded at 612.5 ± 7.5 nm, with sequential excitation and an open pinhole (5 airy units for seedling maps, ×10 lens; 3 airy units for subcellular localization, ×40 lens). Chlorophyll fluorescence was collected at 650 to 700 nm after excitation at 575 nm. To analyze cytosolic and nuclear sensor ratios in regions of interest (ROIs), images were recorded using an LSM980 inverted microscope (Carl Zeiss Microscopy) equipped with a ×40 lens (C-Apochromat, 1.20 numerical aperture, water immersion). tS fluorescence excited at 405 nm was recorded at 517 ± 9 nm and mC fluorescence excited at 561 nm was recorded at 615 ± 9 nm, with sequential excitation and the pinhole set to 2 airy units. Plants were dark adapted for at least 90 min before image acquisition. Single plane images were processed with custom MATLAB-based software (MathWorks; Fricker, 2016) using x,y noise filtering and fluorescence background subtraction.

Statistical Analysis

Statistical analysis and curve fitting were performed as described in the figure legends using the software Prism (version 8.0.1; GraphPad; Supplemental Data Set 1). To investigate statistically significant phenotypic differences between genotypes, and tissue-specific differences in the NAD redox state between different growth conditions, two-way ANOVA followed by the Tukey test was performed. Differences in sensor-specific K_d-values in response to NADH and NADPH were determined by sigmoidal curve fitting. Kinetics were analyzed by nonlinear or linear regression analysis as specified in Supplemental Data Set 1.

Supplemental Data

Supplemental Figure 1. Phenotypic characterization of plants of three independent Arabidopsis biosensor lines expressing Peredox-mCherry in the cytosol compared with the wild-type control.

Supplemental Figure 2. Optimization of protein overexpression and purification of Peredox-mCherry.

Supplemental Figure 3. Response of Peredox-mCherry to increasing NAD(P)H concentrations.

Supplemental Figure 4. Peredox-mCherry fluorescence in Arabidopsis seedlings.

Supplemental Figure 5. In vivo fluorescence spectra of three independent Peredox-mCherry lines.

Supplemental Figure 6. In vivo live interventions of cytosolic NAD redox dynamics in seedlings and leaf discs of independent sensor lines.

Supplemental Figure 7. In vitro responses of Peredox-mCherry DS to NADH and NADH/NAD^+.

Supplemental Figure 8. Peredox-mCherry DS expression in *Arabidopsis thaliana* biosensor lines.

Supplemental Figure 9. In vivo NAD redox dynamics of three independent Peredox-mCherry DS lines compared with Peredox-mCherry in response to changes in respiratory activity and external sugar supply.

Supplemental Table. Oligonucleotides used for cloning and mutagenesis.

Supplemental Data Set 1. Statistical analyses.

ACKNOWLEDGMENTS

We thank the Imaging Network of the University of Münster (RI_00497) and Jörg Kudla for access to the Leica SP8 confocal microscope system; Sonja Raetz, Martin Bonin, and Eva Regel for help with protein purification; and Thomas Nietzel and Richard Jaeger for preliminary optimizations of the flg22 experiments. We further thank the reviewers for adding important thoughts to this article and Alberto P. Macho for stimulating exchange on

the role of NAD in immunity signaling. This work was supported by the Deutsche Forschungsgemeinschaft through the priority program SPP1710 "Dynamics of thiol-based redox switches in cellular physiology" SCHW1719/7-1, the infrastructure grant INST211/903-1 FUGG, and the project grant SCHW1719/5-1 as part of the package PAK918.

AUTHOR CONTRIBUTIONS

J.S., S.W., and M.S. designed research; J.S., P.F., Y.L.N., M.E, S.L., Y.S., E.F.-A., J.B.K., J.-O.N., C.H., S.W., and M.S. performed the experiments; J.S., P.F., Y.L.N., M.E., S.L., E.F.-A., J.B.K., J.-O.N., C.H., E.N.S., M.M., A.N.-N., A.J.M., M.Z., B.M., S.W., and M.S. analyzed data; A.N.-N., A.J.M., M.Z., B.M., S.W., and M.S. supervised the research; J.S. and M.S. wrote the article with input from all coauthors.

Received March 25, 2020; revised July 13, 2020; accepted August 12, 2020; published October 13, 2020.

REFERENCES

Albrecht, S.C., Barata, A.G., Grosshans, J., Teleman, A.A., and Dick, T.P. (2011). *In vivo* mapping of hydrogen peroxide and oxidized glutathione reveals chemical and regional specificity of redox homeostasis. Cell Metab. **14:** 819–829.

Aller, I., Rouhier, N., and Meyer, A.J. (2013). Development of roGFP2-derived redox probes for measurement of the glutathione redox potential in the cytosol of severely glutathione-deficient *rml1* seedlings. Front. Plant Sci. **4:** 506.

António, C., Päpke, C., Rocha, M., Diab, H., Limami, A.M., Obata, T., Fernie, A.R., and van Dongen, J.T. (2016). Regulation of primary metabolism in response to low oxygen availability as revealed by carbon and nitrogen isotope redistribution. Plant Physiol. **170:** 43–56.

Bailey-Serres, J. (2013). Microgenomics: Genome-scale, cell-specific monitoring of multiple gene regulation tiers. Annu. Rev. Plant Biol. **64:** 293–325.

Behera, S., Wang, N., Zhang, C., Schmitz-Thom, I., Strohkamp, S., Schültke, S., Hashimoto, K., Xiong, L., and Kudla, J. (2015). Analyses of Ca^{2+} dynamics using a ubiquitin-10 promoter-driven Yellow Cameleon 3.6 indicator reveal reliable transgene expression and differences in cytoplasmic Ca^{2+} responses in Arabidopsis and rice (*Oryza sativa*) roots. New Phytol. **206:** 751–760.

Behera, S., Zhaolong, X., Luoni, L., Bonza, M.C., Doccula, F.G., De Michelis, M.I., Morris, R.J., Schwarzländer, M., and Costa, A. (2018). Cellular Ca^{2+} signals generate defined pH signatures in plants. Plant Cell **30:** 2704–2719.

Bernhardt, K., Wilkinson, S., Weber, A.P.M., and Linka, N. (2012). A peroxisomal carrier delivers NAD^+ and contributes to optimal fatty acid degradation during storage oil mobilization. Plant J. **69:** 1–13.

Beshir, W.F., Tohge, T., Watanabe, M., Hertog, M.L.A.T.M., Hoefgen, R., Fernie, A.R., and Nicolaï, B.M. (2019). Non-aqueous fractionation revealed changing subcellular metabolite distribution during apple fruit development. Hortic. Res. **6:** 98.

Bhat, S.A., Iqbal, I.K., and Kumar, A. (2016). Imaging the NADH: NAD^+ homeostasis for understanding the metabolic response of Mycobacterium to physiologically relevant stresses. Front. Cell. Infect. Microbiol. **6:** 145.

Bilan, D.S., and Belousov, V.V. (2017). New tools for redox biology: From imaging to manipulation. Free Radic. Biol. Med. **109:** 167–188.

Bilan, D.S., Matlashov, M.E., Gorokhovatsky, A.Y., Schultz, C., Enikolopov, G., and Belousov, V.V. (2014). Genetically encoded fluorescent indicator for imaging NAD^+/NADH ratio changes in different cellular compartments. Biochim. Biophys. Acta **1840:** 951–957.

Blacker, T.S., Mann, Z.F., Gale, J.E., Ziegler, M., Bain, A.J., Szabadkai, G., and Duchen, M.R. (2014). Separating NADH and NADPH fluorescence in live cells and tissues using FLIM. Nat. Commun. **5:** 3936.

Boussardon, C., Przybyla-Toscano, J., Carrie, C., and Keech, O. (2020). Tissue-specific isolation of Arabidopsis/plant mitochondria - IMTACT (isolation of mitochondria tagged in specific cell types). Plant J. **103:** 459–473.

Bradford, M.M. (1976). A rapid and sensitive method for the quantitation of microgram quantities of protein utilizing the principle of protein-dye binding. Anal. Biochem. **72:** 248–254.

Brunoud, G., Wells, D.M., Oliva, M., Larrieu, A., Mirabet, V., Burrow, A.H., Beeckman, T., Kepinski, S., Traas, J., Bennett, M.J., and Vernoux, T. (2012). A novel sensor to map auxin response and distribution at high spatio-temporal resolution. Nature **482:** 103–106.

Cambronne, X.A., Stewart, M.L., Kim, D., Jones-Brunette, A.M., Morgan, R.K., Farrens, D.L., Cohen, M.S., and Goodman, R.H. (2016). Biosensor reveals multiple sources for mitochondrial NAD^+. Science **352:** 1474–1477.

Canepa, L., Ferraris, A.M., Miglino, M., and Gaetani, G.F. (1991). Bound and unbound pyridine dinucleotides in normal and glucose-6-phosphate dehydrogenase-deficient erythrocytes. Biochim. Biophys. Acta **1074:** 101–104.

Chance, B., Legallais, V., and Schoener, B. (1962). Metabolically linked changes in fluorescence emission spectra of cortex of rat brain, kidney and adrenal gland. Nature **195:** 1073–1075.

Chaouch, S., Queval, G., and Noctor, G. (2012). AtRbohF is a crucial modulator of defence-associated metabolism and a key actor in the interplay between intracellular oxidative stress and pathogenesis responses in Arabidopsis. Plant J. **69:** 613–627.

Christensen, C.E., Karlsson, M., Winther, J.R., Jensen, P.R., and Lerche, M.H. (2014). Non-invasive in-cell determination of free cytosolic [NAD^+]/[NADH] ratios using hyperpolarized glucose show large variations in metabolic phenotypes. J. Biol. Chem. **289:** 2344–2352.

Clough, S.J., and Bent, A.F. (1998). Floral dip: A simplified method for Agrobacterium-mediated transformation of *Arabidopsis thaliana*. Plant J. **16:** 735–743.

De Col, V., et al. (2017). ATP sensing in living plant cells reveals tissue gradients and stress dynamics of energy physiology. eLife **6:** 1–29.

Coleman, J.O., and Palmer, J.M. (1972). The oxidation of malate by isolated plant mitochondria. Eur. J. Biochem. **26:** 499–509.

Curtis, M.D., and Grossniklaus, U. (2003). A gateway cloning vector set for high-throughput functional analysis of genes in planta. Plant Physiol. **133:** 462–469.

Dell'Aglio, E., Giustini, C., Kraut, A., Couté, Y., Costa, A., Decros, G., Gibon, Y., Mazars, C., Matringe, M., Finazzi, G., and Curien, G. (2019). Identification of the Arabidopsis calmodulin-dependent NAD^+ kinase that sustains the elicitor-induced oxidative burst. Plant Physiol. **181:** 1449–1458.

van Dongen, J.T., Gupta, K.J., Ramírez-Aguilar, S.J., Araújo, W.L., Nunes-Nesi, A., and Fernie, A.R. (2011). Regulation of respiration in plants: A role for alternative metabolic pathways. J. Plant Physiol. **168:** 1434–1443.

van Dongen, J.T., Schurr, U., Pfister, M., and Geigenberger, P. (2003). Phloem metabolism and function have to cope with low internal oxygen. Plant Physiol. **131:** 1529–1543.

Douce, R., Mannella, C.A., and Bonner, W.D. (1973). The external NADH dehydrogenases of intact plant mitochondria. Biochim. Biophys. Acta Bioenerg. **292:** 105–116.

Eberhard, S., Finazzi, G., and Wollman, F.A. (2008). The dynamics of photosynthesis. Annu. Rev. Genet. **42:** 463–515.

Feitosa-Araujo, E., et al. (2020). Downregulation of a mitochondrial NAD^+ transporter (NDT2) alters seed production and germination in Arabidopsis. Plant Cell Physiol. **61:** 897–908.

Felle, H.H. (2001). pH: Signal and messenger in plant cells. Plant Biol. **3:** 577–591.

Fernie, A.R., Carrari, F., and Sweetlove, L.J. (2004). Respiratory metabolism: Glycolysis, the TCA cycle and mitochondrial electron transport. Curr. Opin. Plant Biol. **7:** 254–261.

Fricker, M.D. (2016). Quantitative redox imaging software. Antioxid. Redox Signal. **24:** 752–762.

Fuchs, P., et al. (2020). Single organelle function and organization as estimated from Arabidopsis mitochondrial proteomics. Plant J. **101:** 420–441.

Fürtauer, L., Weckwerth, W., and Nägele, T. (2016). A benchtop fractionation procedure for subcellular analysis of the plant metabolome. Front. Plant Sci. **7:** 1912.

Gakière, B., Hao, J., de Bont, L., Pétriacq, P., Nunes-Nesi, A., and Fernie, A.R. (2018). NAD^+ biosynthesis and signaling in plants. Crit. Rev. Plant Sci. **37:** 259–307.

Geigenberger, P. (2003). Response of plant metabolism to too little oxygen. Curr. Opin. Plant Biol. **6:** 247–256.

Hartmann, S.K., Stockdreher, Y., Wandrey, G., Hosseinpour, H., Zambanini, T., Meyer, A.J., Büchs, J., Blank, L.M., Schwarzländer, M., and Wierckx, N. (2018). Online *in vivo* monitoring of cytosolic NAD redox dynamics in *Ustilago maydis*. Biochim. Biophys. Acta Bioenerg. **1859:** 1015–1024.

Hashida, S.N., Itami, T., Takahashi, H., Takahara, K., Nagano, M., Kawai-Yamada, M., Shoji, K., Goto, F., Yoshihara, T., and Uchimiya, H. (2010). Nicotinate/nicotinamide mononucleotide adenyltransferase-mediated regulation of NAD biosynthesis protects guard cells from reactive oxygen species in ABA-mediated stomatal movement in Arabidopsis. J. Exp. Bot. **61:** 3813–3825.

Hashida, S.N., Takahashi, H., Kawai-Yamada, M., and Uchimiya, H. (2007). *Arabidopsis thaliana* nicotinate/nicotinamide mononucleotide adenyltransferase (AtNMNAT) is required for pollen tube growth. Plant J. **49:** 694–703.

Hatch, M.D., Dröscher, L., Flügge, U.I., and Heldt, H.W. (1984). A specific translocator for oxaloacetate transport in chloroplasts. FEBS Lett. **178:** 15–19.

Heber, U. (1974). Metabolite exchange between chloroplasts and cytoplasm. Annu. Rev. Plant Physiol. **25:** 393–421.

Heineke, D., Riens, B., Grosse, H., Hoferichter, P., Peter, U., Flügge, U.I., and Heldt, H.W. (1991). Redox transfer across the inner chloroplast envelope membrane. Plant Physiol. **95:** 1131–1137.

Hong, Y., Wang, Z., Shi, H., Yao, J., Liu, X., Wang, F., Zeng, L., Xie, Z., and Zhu, J.K. (2020). Reciprocal regulation between nicotinamide adenine dinucleotide metabolism and abscisic acid and stress response pathways in Arabidopsis. PLoS Genet. **16:** e1008892.

Horsefield, S., et al. (2019). NAD^+ cleavage activity by animal and plant TIR domains in cell death pathways. Science **365:** 793–799.

Hung, Y.P., Albeck, J.G., Tantama, M., and Yellen, G. (2011). Imaging cytosolic NADH-NAD^+ redox state with a genetically encoded fluorescent biosensor. Cell Metab. **14:** 545–554.

Hunt, L., Holdsworth, M.J., and Gray, J.E. (2007). Nicotinamidase activity is important for germination. Plant J. **51:** 341–351.

Igamberdiev, A.U., and Gardeström, P. (2003). Regulation of NAD- and NADP-dependent isocitrate dehydrogenases by reduction levels of pyridine nucleotides in mitochondria and cytosol of pea leaves. Biochim. Biophys. Acta **1606:** 117–125.

Ishikawa, M., Tanaka, Y., Suzuki, R., Kimura, K., Tanaka, K., Kamiya, K., Ito, H., Kato, S., Kamachi, T., Hori, K., and Nakanishi, S. (2017). Real-time monitoring of intracellular redox changes in *Methylococcus capsulatus* (Bath) for efficient bioconversion of methane to methanol. Bioresour. Technol. **241:** 1157–1161.

Jones, A.M., Danielson, J.Å., Manojkumar, S.N., Lanquar, V., Grossmann, G., and Frommer, W.B. (2014). Abscisic acid dynamics in roots detected with genetically encoded FRET sensors. eLife **3:** e01741.

Kadota, Y., Sklenar, J., Derbyshire, P., Stransfeld, L., Asai, S., Ntoukakis, V., Jones, J.D., Shirasu, K., Menke, F., Jones, A., and Zipfel, C. (2014). Direct regulation of the NADPH oxidase RBOHD by the PRR-associated kinase BIK1 during plant immunity. Mol. Cell **54:** 43–55.

Kasimova, M.R., Grigiene, J., Krab, K., Hagedorn, P.H., Flyvbjerg, H., Andersen, P.E., and Møller, I.M. (2006). The free NADH concentration is kept constant in plant mitochondria under different metabolic conditions. Plant Cell **18:** 688–698.

Kawai, S., and Murata, K. (2008). Structure and function of NAD kinase and NADP phosphatase: key enzymes that regulate the intracellular balance of NAD(H) and NADP(H). Biosci. Biotechnol. Biochem. **72:** 919–930.

Kinoshita, H., Nagasaki, J., Yoshikawa, N., Yamamoto, A., Takito, S., Kawasaki, M., Sugiyama, T., Miyake, H., Weber, A.P.M., and Taniguchi, M. (2011). The chloroplastic 2-oxoglutarate/malate transporter has dual function as the malate valve and in carbon/nitrogen metabolism. Plant J. **65:** 15–26.

Laurino, P., Tóth-Petróczy, Á., Meana-Pañeda, R., Lin, W., Truhlar, D.G., and Tawfik, D.S. (2016). An ancient fingerprint indicates the common ancestry of Rossmann-fold enzymes utilizing different ribose-based cofactors. PLoS Biol. **14:** e1002396.

Lee, C.P., and Millar, A.H. (2016). The plant mitochondrial transportome: Balancing metabolic demands with energetic constraints. Trends Plant Sci. **21:** 662–676.

Li, B.B., Wang, X., Tai, L., Ma, T.T., Shalmani, A., Liu, W.T., Li, W.Q., and Chen, K.M. (2018). NAD kinases: Metabolic targets controlling redox co-enzymes and reducing power partitioning in plant stress and development. Front. Plant Sci. **9:** 379.

Li, S., Yamada, M., Han, X., Ohler, U., and Benfey, P.N. (2016). High-resolution expression map of the Arabidopsis root reveals alternative splicing and lincRNA regulation. Dev. Cell **39:** 508–522.

Lim, S.L., Voon, C.P., Guan, X., Yang, Y., Gardeström, P., and Lim, B.L. (2020). In planta study of photosynthesis and photorespiration using NADPH and NADH/NAD^+ fluorescent protein sensors. Nat. Commun. **11:** 3238.

Lu, W., Wang, L., Chen, L., Hui, S., and Rabinowitz, J.D. (2018). Extraction and quantitation of nicotinamide adenine dinucleotide redox cofactors. Antioxidants Redox Signal. **28:** 167–179.

Luo, L., He, Y., Xu, Q., Lyu, W., Yan, J., Xin, P., Zhang, D., Chu, J., Li, J., and Yu, H. (2020). Rapid and specific isolation of intact mitochondria from Arabidopsis leaves. J. Genet. Genomics **47:** 65–68.

Luo, L., He, Y., Zhao, Y., Xu, Q., Wu, J., Ma, H., Guo, H., Bai, L., Zuo, J., Zhou, J.M., Yu, H., and Li, J. (2019). Regulation of mitochondrial NAD pool via NAD^+ transporter 2 is essential for matrix NADH homeostasis and ROS production in Arabidopsis. Sci. China Life Sci. **62:** 991–1002.

Macho, A.P., Boutrot, F., Rathjen, J.P., and Zipfel, C. (2012). ASPARTATE OXIDASE plays an important role in Arabidopsis stomatal immunity. Plant Physiol. **159:** 1845–1856.

Medeiros, D., Arrivault, S., Alpers, J., Fernie, A., and Aarabi, F. (2019). Non-aqueous fractionation (NAF) for metabolite analysis in subcellular compartments of Arabidopsis leaf tissues. Bio Protoc. **9:** 1–19.

Michalecka, A.M., Svensson, Å.S., Johansson, F.I., Agius, S.C., Johanson, U., Brennicke, A., Binder, S., and Rasmusson, A.G. (2003). Arabidopsis genes encoding mitochondrial type II NAD(P)H

dehydrogenases have different evolutionary origin and show distinct responses to light. Plant Physiol. **133:** 642–652.

Møller, I.M., Igamberdiev, A.U., Bykova, N.V., Finkemeier, I., Rasmusson, A.G., and Schwarzländer, M. (2020). Matrix redox physiology governs the regulation of plant mitochondrial metabolism through posttranslational protein modifications. Plant Cell **32:** 573–594.

Mühling, K.H., Plieth, C., Hansen, U.P., and Sattelmacher, B. (1995). Apoplastic pH of intact leaves of *Vicia faba* as influenced by light. J. Exp. Bot. **46:** 377–382.

Murashige, T., and Skoog, F. (1962). A revised medium for rapid growth and biol. assays with tobaoco tissue cultures. Physiol. Plant. **15:** 473–497.

Nietzel, T., et al. (2019). The fluorescent protein sensor roGFP2-Orp1 monitors *in vivo* H_2O_2 and thiol redox integration and elucidates intracellular H_2O_2 dynamics during elicitor-induced oxidative burst in Arabidopsis. New Phytol. **221:** 1649–1664.

Noctor, G. (2006). Metabolic signalling in defence and stress: The central roles of soluble redox couples. Plant Cell Environ. **29:** 409–425.

Noctor, G., Queval, G., and Gakière, B. (2006). NAD(P) synthesis and pyridine nucleotide cycling in plants and their potential importance in stress conditions. J. Exp. Bot. **57:** 1603–1620.

Pak, V.V., et al. (2020). Ultrasensitive genetically encoded indicator for hydrogen peroxide identifies roles for the oxidant in cell migration and mitochondrial function. Cell Metab. **31:** 642–653.e6.

Palmer, A.E., and Tsien, R.Y. (2006). Measuring calcium signaling using genetically targetable fluorescent indicators. Nat. Protoc. **1:** 1057–1065.

Palmieri, F., et al. (2009). Molecular identification and functional characterization of *Arabidopsis thaliana* mitochondrial and chloroplastic NAD^+ carrier proteins. J. Biol. Chem. **284:** 31249–31259.

Pétriacq, P., de Bont, L., Hager, J., Didierlaurent, L., Mauve, C., Guérard, F., Noctor, G., Pelletier, S., Renou, J.P., Tcherkez, G., and Gakière, B. (2012). Inducible NAD overproduction in Arabidopsis alters metabolic pools and gene expression correlated with increased salicylate content and resistance to *Pst-AvrRpm1*. Plant J. **70:** 650–665.

Pétriacq, P., Ton, J., Patrit, O., Tcherkez, G., and Gakière, B. (2016). NAD acts as an integral regulator of multiple defense layers. Plant Physiol. **172:** 1465–1479.

Queval, G., and Noctor, G. (2007). A plate reader method for the measurement of NAD, NADP, glutathione, and ascorbate in tissue extracts: Application to redox profiling during Arabidopsis rosette development. Anal. Biochem. **363:** 58–69.

Rasmusson, A.G., Geisler, D.A., and Møller, I.M. (2008). The multiplicity of dehydrogenases in the electron transport chain of plant mitochondria. Mitochondrion **8:** 47–60.

Rasmusson, A.G., Soole, K.L., and Elthon, T.E. (2004). Alternative NAD(P)H dehydrogenases of plant mitochondria. Annu. Rev. Plant Biol. **55:** 23–39.

Renné, P., Dressen, U., Hebbeker, U., Hille, D., Flügge, U.I., Westhoff, P., and Weber, A.P.M. (2003). The Arabidopsis mutant *dct* is deficient in the plastidic glutamate/malate translocator DiT2. Plant J. **35:** 316–331.

Rich-Griffin, C., Stechemesser, A., Finch, J., Lucas, E., Ott, S., and Schäfer, P. (2020). Single-cell transcriptomics: A high-resolution avenue for plant functional genomics. Trends Plant Sci. **25:** 186–197.

Rizza, A., Walia, A., Lanquar, V., Frommer, W.B., and Jones, A.M. (2017). *In vivo* gibberellin gradients visualized in rapidly elongating tissues. Nat. Plants **3:** 803–813.

Sallin, O., Reymond, L., Gondrand, C., Raith, F., Koch, B., and Johnsson, K. (2018). Semisynthetic biosensors for mapping cellular concentrations of nicotinamide adenine dinucleotides. eLife **7:** 1–32.

Scheibe, R., and Jacquot, J.P. (1983). NADP regulates the light activation of NADP-dependent malate dehydrogenase. Planta **157:** 548–553.

Schippers, J.H.M., Nunes-Nesi, A., Apetrei, R., Hille, J., Fernie, A.R., and Dijkwel, P.P. (2008). The *Arabidopsis onset of leaf death5* mutation of quinolinate synthase affects nicotinamide adenine dinucleotide biosynthesis and causes early ageing. Plant Cell **20:** 2909–2925.

Schwarzländer, M., et al. (2014). The 'mitoflash' probe cpYFP does not respond to superoxide. Nature **514:** E12–E14.

Schwarzländer, M., Dick, T.P., Meyer, A.J., and Morgan, B. (2016). Dissecting redox biology using fluorescent protein sensors. Antioxid. Redox Signal. **24:** 680–712.

Schwarzländer, M., Fricker, M.D., Müller, C., Marty, L., Brach, T., Novak, J., Sweetlove, L.J., Hell, R., and Meyer, A.J. (2008). Confocal imaging of glutathione redox potential in living plant cells. J. Microsc. **231:** 299–316.

Schwarzländer, M., Logan, D.C., Fricker, M.D., and Sweetlove, L.J. (2011). The circularly permuted yellow fluorescent protein cpYFP that has been used as a superoxide probe is highly responsive to pH but not superoxide in mitochondria: implications for the existence of superoxide 'flashes'. Biochem. J. **437:** 381–387.

Schwarzländer, M., Logan, D.C., Johnston, I.G., Jones, N.S., Meyer, A.J., Fricker, M.D., and Sweetlove, L.J. (2012). Pulsing of membrane potential in individual mitochondria: A stress-induced mechanism to regulate respiratory bioenergetics in Arabidopsis. Plant Cell **24:** 1188–1201.

Selinski, J., and Scheibe, R. (2019). Malate valves: Old shuttles with new perspectives. Plant Biol (Stuttg) **21** (Suppl 1): 21–30.

Shameer, S., Ratcliffe, R.G., and Sweetlove, L.J. (2019). Leaf energy balance requires mitochondrial respiration and export of chloroplast NADPH in the light. Plant Physiol. **180:** 1947–1961.

Shaw, S.L., and Ehrhardt, D.W. (2013). Smaller, faster, brighter: Advances in optical imaging of living plant cells. Annu. Rev. Plant Biol. **64:** 351–375.

de Souza Chaves, I., et al. (2019). The mitochondrial NAD^+ transporter (NDT1) plays important roles in cellular NAD^+ homeostasis in *Arabidopsis thaliana*. Plant J. **100:** 487–504.

Sun, F., Dai, C., Xie, J., and Hu, X. (2012). Biochemical issues in estimation of cytosolic free NAD/NADH ratio. PLoS One **7:** e34525.

Sweetlove, L.J., Taylor, N.L., and Leaver, C.J. (2007). Isolation of intact, functional mitochondria from the model plant *Arabidopsis thaliana*. Methods Mol. Biol. **372:** 125–136.

Szal, B., Dąbrowska, Z., Malmberg, G., Gardeström, P., and Rychter, A.M. (2008). Changes in energy status of leaf cells as a consequence of mitochondrial genome rearrangement. Planta **227:** 697–706.

Tadege, M., Dupuis, I., and Kuhlemeier, C. (1999). Ethanolic fermentation: New functions for an old pathway. Trends Plant Sci. **4:** 320–325.

Taniguchi, M., and Miyake, H. (2012). Redox-shuttling between chloroplast and cytosol: Integration of intra-chloroplast and extra-chloroplast metabolism. Curr. Opin. Plant Biol. **15:** 252–260.

Tao, R., et al. (2017). Genetically encoded fluorescent sensors reveal dynamic regulation of NADPH metabolism. Nat. Methods **14:** 720–728.

Tejwani, V., Schmitt, F., Wilkening, S., Zebger, I., Horch, M., Lenz, O., and Friedrich, T. (2017). Investigation of the NADH/NAD^+ ratio in *Ralstonia eutropha* using the fluorescence reporter protein Peredox. Biochim. Biophys. Acta Bioenerg. **1858:** 86–94.

Waadt, R., Hitomi, K., Nishimura, N., Hitomi, C., Adams, S.R., Getzoff, E.D., and Schroeder, J.I. (2014). FRET-based reporters for the direct visualization of abscisic acid concentration changes and distribution in Arabidopsis. eLife **3:** e01739.

Wagner, S., et al. (2019). Multiparametric real-time sensing of cytosolic physiology links hypoxia responses to mitochondrial electron transport. New Phytol. **224:** 1668–1684.

Wagner, S., Van Aken, O., Elsässer, M., and Schwarzländer, M. (2018). Mitochondrial energy signaling and its role in the low-oxygen stress response of plants. Plant Physiol. **176:** 1156–1170.

Wagner, S., Nietzel, T., Aller, I., Costa, A., Fricker, M.D., Meyer, A.J., and Schwarzländer, M. (2015). Analysis of plant mitochondrial function using fluorescent protein sensors. Methods Mol. Biol. **1305:** 241–252.

Wagner, S., Stuttmann, J., Rietz, S., Guerois, R., Brunstein, E., Bautor, J., Niefind, K., and Parker, J.E. (2013). Structural basis for signaling by exclusive EDS1 heteromeric complexes with SAG101 or PAD4 in plant innate immunity. Cell Host Microbe **14:** 619–630.

Waller, J.C., Dhanoa, P.K., Schumann, U., Mullen, R.T., and Snedden, W.A. (2010). Subcellular and tissue localization of NAD kinases from Arabidopsis: Compartmentalization of *de novo* NADP biosynthesis. Planta **231:** 305–317.

Wan, L., Essuman, K., Anderson, R.G., Sasaki, Y., Monteiro, F., Chung, E.H., Osborne Nishimura, E., DiAntonio, A., Milbrandt, J., Dangl, J.L., and Nishimura, M.T. (2019). TIR domains of plant immune receptors are NAD^+-cleaving enzymes that promote cell death. Science **365:** 799–803.

Wang, C., Huang, X., Li, Q., Zhang, Y., Li, J.L., and Mou, Z. (2019). Extracellular pyridine nucleotides trigger plant systemic immunity through a lectin receptor kinase/BAK1 complex. Nat. Commun. **10:** 4810.

Wang, C., Zhou, M., Zhang, X., Yao, J., Zhang, Y., and Mou, Z. (2017). A lectin receptor kinase as a potential sensor for extracellular nicotinamide adenine dinucleotide in *Arabidopsis thaliana*. eLife **6:** 1–23.

Weber, A., and Flügge, U.I. (2002). Interaction of cytosolic and plastidic nitrogen metabolism in plants. J. Exp. Bot. **53:** 865–874.

Wei, M., Zhuang, Y., Li, H., Li, P., Huo, H., Shu, D., Huang, W., and Wang, S. (2020). The cloning and characterization of hypersensitive to salt stress mutant, affected in quinolinate synthase, highlights the involvement of NAD in stress-induced accumulation of ABA and proline. Plant J. **102:** 85–98.

Weits, D.A., Kunkowska, A.B., Kamps, N.C.W., Portz, K.M.S., Packbier, N.K., Nemec Venza, Z., Gaillochet, C., Lohmann, J.U., Pedersen, O., van Dongen, J.T., and Licausi, F. (2019). An apical hypoxic niche sets the pace of shoot meristem activity. Nature **569:** 714–717.

Wiermer, M., Feys, B.J., and Parker, J.E. (2005). Plant immunity: The EDS1 regulatory node. Curr. Opin. Plant Biol. **8:** 383–389.

Wigge, B., Krömer, S., and Gardeström, P. (1993). The redox levels and subcellular distribution of pyridine nucleotides in illuminated barley leaf protoplasts studied by rapid fractionation. Physiol. Plant. **88:** 10–18.

Wilcox, M., and Moreland, D.E. (1969). Herbicide 4-(3,4-dichlorophenyl)-1,1,2-trimethylsemicarbazide and its mechanism of action. Nature **222:** 878–879.

Williamson, D.H., Lund, P., and Krebs, H.A. (1967). The redox state of free nicotinamide-adenine dinucleotide in the cytoplasm and mitochondria of rat liver. Biochem. J. **103:** 514–527.

Wolosiuk, R.A., Buchanan, B.B., and Crawford, N.A. (1977). Regulation of NADP-malate dehydrogenase by the light-actuated ferredoxin/thioredoxin system of chloroplasts. FEBS Lett. **81:** 253–258.

Yin, Z.H., Neimanis, S., Wagner, U., and Heber, U. (1990). Light-dependent pH changes in leaves of C3 plants: I. Recording pH changes in various cellular compartments by fluorescent probes. Planta **182:** 244–252.

Zhang, X., and Mou, Z. (2009). Extracellular pyridine nucleotides induce PR gene expression and disease resistance in Arabidopsis. Plant J. **57:** 302–312.

Zhang, Z.S., Liu, M.J., Scheibe, R., Selinski, J., Zhang, L.T., Yang, C., Meng, X.L., and Gao, H.Y. (2017). Contribution of the alternative respiratory pathway to PSII photoprotection in C3 and C4 plants. Mol. Plant **10:** 131–142.

Zhao, Y., et al. (2015). SoNar, a highly responsive NAD^+/NADH sensor, allows high-throughput metabolic screening of anti-tumor agents. Cell Metab. **21:** 777–789.

Zhao, Y., Jin, J., Hu, Q., Zhou, H.M., Yi, J., Yu, Z., Xu, L., Wang, X., Yang, Y., and Loscalzo, J. (2011). Genetically encoded fluorescent sensors for intracellular NADH detection. Cell Metab. **14:** 555–566.

Zoglowek, C., Krömer, S., and Heldt, H.W. (1988). Oxaloacetate and malate transport by plant mitochondria. Plant Physiol. **87:** 109–115.

Zou, Y., et al. (2020). Illuminating NAD^+ metabolism in live cells and *in vivo* using a genetically encoded fluorescent sensor. Dev. Cell **53:** 240–252.e7.